



# Topological frequency combs and nested temporal solitons

Sunil Mittal<sup>1,2</sup>✉, Gregory Moille<sup>1,3</sup>, Kartik Srinivasan<sup>1,3</sup>, Yanne K. Chembo<sup>2</sup> and Mohammad Hafezi<sup>1,2,4</sup>

**Recent advances in realizing optical frequency combs using nonlinear parametric processes in integrated photonic resonators have revolutionized on-chip optical clocks, spectroscopy and multichannel optical communications. At the same time, the introduction of topological physics in photonic systems has allowed the design of photonic devices with novel functionalities and inherent robustness against fabrication disorders. Here we use topological design principles to theoretically propose the generation of optical frequency combs and temporal dissipative Kerr solitons in a two-dimensional array of coupled ring resonators that creates a synthetic magnetic field for photons and exhibits topological edge states. We show that these topological edge states constitute a travelling-wave super-ring resonator that leads to the generation of coherent nested optical frequency combs, as well as the self-formation of nested temporal solitons and Turing rolls that are remarkably phase-locked over more than 40 rings. Moreover, we show that the topological nested solitons are robust against defects in the lattice, and a single nested soliton achieves a mode efficiency of over 50%, an order of magnitude higher than single-ring frequency combs. Our topological frequency comb works in a parameter regime that can be readily accessed using existing low-loss integrated photonic platforms like silicon nitride.**

While optical frequency combs naturally emerge in mode-locked ultrafast lasers<sup>1–3</sup>, the use of nonlinear parametric processes—particularly the Kerr effect—in integrated photonic resonators offers a much more convenient and compact route to generate optical frequency combs<sup>4–8</sup>. Of particular significance is the regime of coherent optical frequency combs where the intrinsic dispersion and dissipation of a photonic resonator are counterbalanced by nonlinearity-induced dispersion and parametric gain, respectively, and this double-balance leads to the self-formation of stationary temporal solutions called dissipative Kerr solitons (DKSs)<sup>5</sup>. DKSs have been demonstrated in a variety of single-resonator geometries, and diverse material platforms such as silica glass, silicon nitride, and so on<sup>5,6,9</sup>. More recently, DKSs have been explored in photonic molecules, that is, a configuration of two coupled resonators, which allows the exploration of collective coherence or self-organization of solitons as well as solitonic solutions that are inaccessible using a single resonator<sup>10–13</sup>.

In parallel, advances in the field of topological photonics have allowed access to new paradigms that can be used to design photonic devices with novel functionalities<sup>14–16</sup>. On one hand, topological photonic systems use complex arrays of hundreds of coupled waveguides or ring resonators<sup>17–19</sup>. On the other hand, such systems exhibit remarkably simple features such as edge states, which are dictated only by the global topology and therefore are independent of local details of the system. This unique property of edge states protects them against local defects and disorders in the system, enabling the realization of robust photonic devices such as optical delay lines<sup>17,18,20</sup>, lasers<sup>21–24</sup>, switches<sup>25,26</sup>, photonic crystal waveguides and cavities<sup>27–29</sup>, fibres<sup>30</sup>, etc. Lately, topological edge states have also been used in conjunction with nonlinear parametric

processes for the efficient and tunable generation of quantum states of light via spontaneous four-wave mixing<sup>31–33</sup>, optical frequency conversion<sup>34,35</sup>, as well as to explore spatial solitons in coupled waveguide arrays<sup>36–39</sup>.

Here we theoretically investigate the generation of coherent optical frequency combs and temporal DKSs in a topological photonic system consisting of a two-dimensional lattice of coupled (micro)ring resonators. We exploit the fact that the topological edge states circulate around the boundary of the lattice, and because of their unidirectionality, they constitute a travelling-wave super-ring resonator formed of multiple single-ring resonators (Fig. 1e). We show that pumping the edge state super-ring resonator with a continuous-wave (CW) laser—of optimal frequency and power—leads to the self-formation of temporal patterns, particularly Turing rolls and nested DKSs. More importantly, these temporal patterns are phase-locked across all the ring resonators on the edge of the lattice, indicating collective coherence or self-organization across more than 40 oscillators. In the regime of nested solitons, the spectral output of our device corresponds to that of a coherent nested optical frequency comb (Fig. 1f). We find that the nested solitons inherit the topological protection of a linear system and are robust against any defects in the lattice. From an application perspective, in the regime of a single nested soliton, the topological frequency comb achieves a mode efficiency of >50%, an order of magnitude higher than single-ring frequency combs<sup>40–42</sup> that are theoretically limited to only ~5%. Our design can be readily implemented with the existing nanofabrication technology (Supplementary Section 3), and similar topological ring resonator systems with nonlinear parametric processes have already been realized to enhance and engineer the generation of quantum states of light<sup>31,32</sup>.

<sup>1</sup>Joint Quantum Institute, National Institute of Standards and Technology/University of Maryland, College Park, MD, USA. <sup>2</sup>Department of Electrical and Computer Engineering and IREAP, University of Maryland, College Park, MD, USA. <sup>3</sup>Microsystems and Nanotechnology Division, Physical Measurement Laboratory, National Institute of Standards and Technology, Gaithersburg, MD, USA. <sup>4</sup>Department of Physics, University of Maryland, College Park, MD, USA. ✉e-mail: [mittals@umd.edu](mailto:mittals@umd.edu)

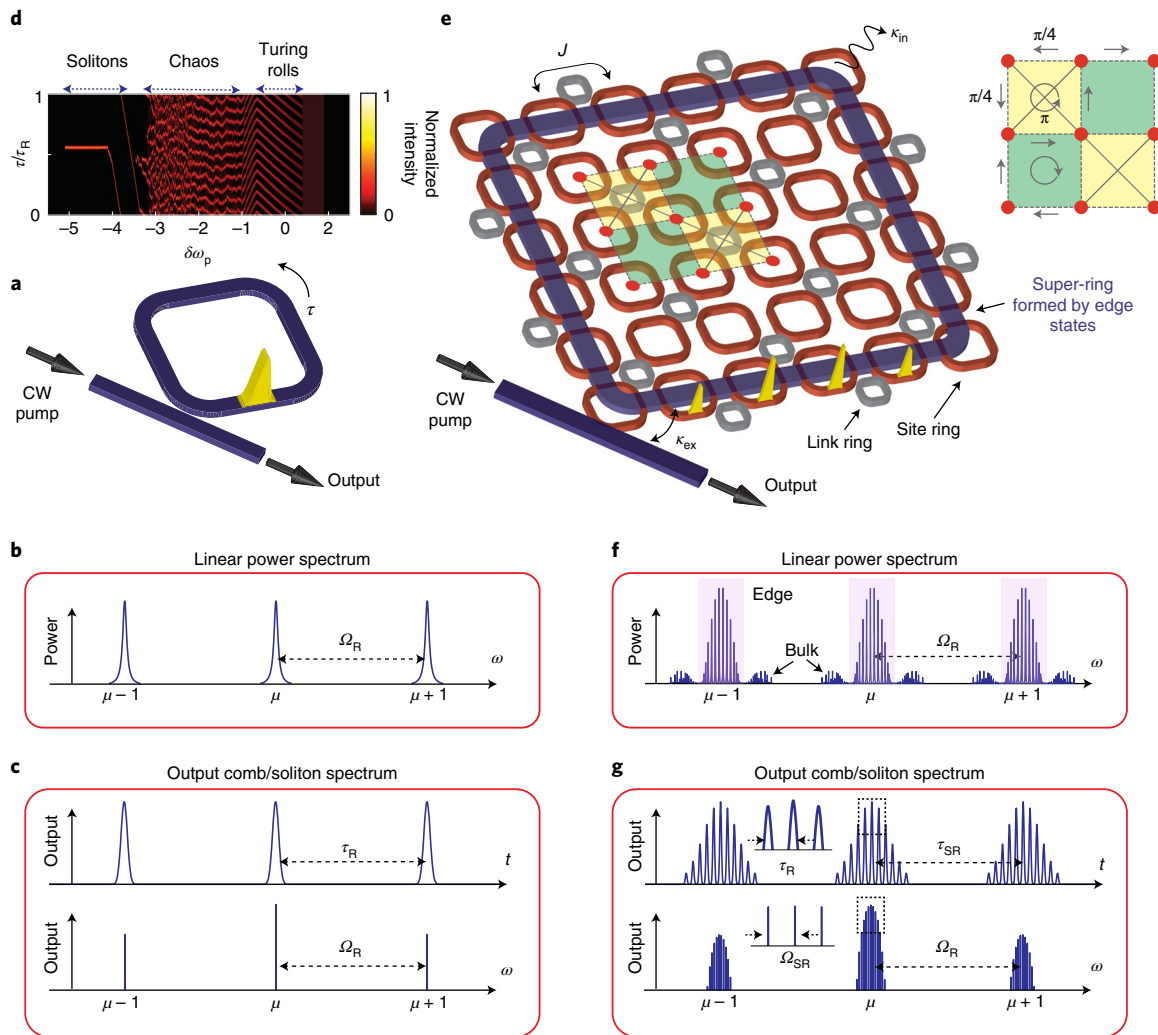


**Fig. 1 | Working of the topological frequency comb.** **a, b**, Schematic of a single-ring resonator (**a**) and its power spectrum in the linear regime (**b**). **c**, Temporal and spectral response at the output of the ring resonator in the regime of a single Kerr soliton. The temporal output consists of a series of pulses separated by  $\tau_R$ , the round-trip time of the ring resonator. The spectral output consists of a series of narrow lines separated by FSR  $\Omega_R$ . **d**, An indicative spatiotemporal intensity distribution in the ring, showing different operating regimes as a function of input pump frequency detuning  $\delta\omega_p$  from cold-cavity resonance (Supplementary Fig. 3). **e**, Schematic of a two-dimensional array of ring resonators that simulates the anomalous quantum Hall model for photons and exhibits topological edge modes at its boundary. **f**, Power spectrum in the linear regime showing edge state resonances (shaded) and bulk bands. The edge states extend throughout the boundary of the lattice and constitute a super-ring resonator, with longitudinal mode separation  $\Omega_{SR}$ . The transmission spectrum repeats every FSR  $\Omega_R$  of the ring resonators. When pumped by a CW laser near one of the edge mode resonances, the topological super-ring can host nested solitons with indicative spatial intensity profile shown by yellow-coloured pulses. **g**, Schematic of the temporal and spectral output of the topological frequency comb in the regime of a single nested soliton. The output temporal profile consists of a series of soliton pulses separated by single-ring round-trip time  $\tau_R$  (fast time), modulated by a series of super-soliton pulses separated by the round-trip time  $\tau_{SR}$  (slow time) of the edge mode super-ring. The output spectral profile shows a nested comb, that is, a series (comb) of edge mode resonances (longitudinal modes of the super-ring; slow frequency) oscillating in each FSR (fast frequency) of the the single-ring resonators.

### Topological system and simulation framework

Our topological system consists of a square lattice with a site-ring resonator located at each of its lattice sites (Fig. 1e)<sup>43,44</sup> (Supplementary Section 1). The site-ring resonators are coupled to their nearest and next-nearest neighbours, using another set of link rings, such that a non-zero local synthetic magnetic field for photons with flux  $\pi$  threads a half-unit cell, but the flux threading a complete unit cell is zero. Close to a given longitudinal mode resonance of the site rings, the lattice simulates a Haldane-like anomalous quantum Hall model for photons. Accordingly, its power spectrum (or the energy-momentum band structure) exhibits a topological edge band sandwiched between two bulk bands (Fig. 1f and Supplementary

Section 1). The edge states propagate all along the boundary of the lattice in a single direction (set by the input port<sup>44</sup>) and therefore constitute a travelling-wave super-ring resonator (Fig. 1e and Supplementary Fig. 1). The multiple longitudinal modes of the super-ring—equally separated in frequency by free spectral range (FSR)  $\Omega_{SR}$ —are clearly evident in the edge band of the power spectrum. Furthermore, this structure of an edge band sandwiched between two bulk bands repeats in frequency every FSR (longitudinal mode spacing  $\Omega_R$ ) of the individual ring resonators. Therefore, our topological system effectively involves three dimensions—two real dimensions in space and one synthetic dimension in frequency that is associated with the longitudinal modes of the ring resonators.

To generate an optical frequency comb in this lattice, we couple one ring at the edge of the lattice to an input–output waveguide, as shown in Fig. 1e. At the input port of this waveguide, we inject a CW pump laser with frequency close to one of the longitudinal mode resonances of the ring resonators (indexed by an integer  $\mu=0$ ). The intrinsic Kerr nonlinearity of the ring resonators leads to spontaneous four-wave mixing and subsequently stimulates the generation of photons in other longitudinal modes ( $\mu \neq 0$ ) in the form of a frequency comb.

To simulate the generation of an optical frequency comb in the lattice, we derive the coupled driven-dissipative nonlinear Schrödinger equations, also called Lugiato–Lefever equations<sup>6,45,46</sup>, which dictate the complete spatial, spectral and temporal evolution of site-ring fields as

$$\begin{aligned} \frac{da_{m,\mu}}{dt} = & -i(\omega_{0,\mu} - \Omega_R \mu - \omega_p) a_{m,\mu} - J \sum_{\langle n \rangle} a_{n,\mu} e^{-i\phi_{m,n}} \\ & - J \sum_{\langle n \rangle} a_{n,\mu} + i\gamma \frac{1}{\tau_R} \int_0^{\tau_R} d\tau (|\tilde{a}_{m,\tau}|^2 \tilde{a}_{m,\tau}) e^{-i\omega_\mu \tau} \\ & - (\kappa_{\text{ex}} \delta_{m,\text{IO}} + \kappa_{\text{in}}) a_{m,\mu} + \delta_{m,\text{IO}} \delta_{\mu,0} \mathcal{E}. \end{aligned} \quad (1)$$

Here  $a_{m,\mu}$  is the photon field for the site ring at spatial position  $m$  for a given longitudinal mode  $\mu$ ;  $J$  is the coupling strength between the ring resonators and is the same for both nearest-neighbour (indicated by  $\langle m,n \rangle$ ) and next-nearest-neighbour (indicated by  $\langle\langle m,n \rangle\rangle$ ) couplings. The hopping phase  $\phi_{m,n} = \pm \frac{\pi}{4}$  for nearest-neighbour couplings and  $\phi_{m,n} = 0$  for the next-nearest-neighbour couplings (Supplementary Section 1). Further,  $\gamma$  is the strength of the nonlinear interaction,  $\kappa_{\text{ex}}$  is the coupling rate of the input–output (IO) ring (indicated by  $\delta_{m,\text{IO}}$ ) to the input–output waveguide, and  $\kappa_{\text{in}}$  is the loss rate of the ring resonators;  $\mathcal{E}$  is the normalized input pump field, which is coupled only to the IO ring, and is in the longitudinal mode  $\mu=0$  (indicated by  $\delta_{\mu,0}$ ). Also,  $\omega_{0,\mu}$  is the resonance frequency of the site-ring resonators for a longitudinal mode with index  $\mu$  and includes second-order anomalous dispersion  $D_2$  such that

$$\omega_{0,\mu} = \omega_0 + \Omega_R \mu + \frac{D_2}{2} \mu^2. \quad (2)$$

The input pump frequency is denoted by  $\omega_p$  and the pumped longitudinal mode corresponds to  $\mu=0$  with resonance frequency  $\omega_0$ . The coupled equations (1) have been written in a reference frame rotating at frequency  $\Omega_R/2\pi$  such that the FSR of the individual ring resonators is an independent parameter (equations (1) and (2)). Also, note that we have not made any assumptions regarding the spectral position, bandwidth or dispersion of the edge state resonances within a longitudinal mode  $\mu$  (Supplementary Section 8).

In equation (1), the nonlinear four-wave mixing interaction between different longitudinal mode resonances is represented in the time domain  $\tau$  (in  $[0, \tau_R]$ ), which corresponds to the round-trip time within a single-ring resonator<sup>47,48</sup>. Specifically, in a reference frame rotating at frequency  $\Omega_R/2\pi = 1/\tau_R$ ,  $\tilde{a}_{m,\tau}$  represents the spatiotemporal field within a ring, at lattice location  $m$ , and is related to the spectral field within the ring as

$$a_{m,\mu} = \frac{1}{\tau_R} \int_0^{\tau_R} d\tau \tilde{a}_{m,\tau} e^{-i\omega_{0,\mu} \tau}. \quad (3)$$

We emphasize that the spectral and temporal dynamics of our system, as dictated by equation (1), involves two disparate frequency and time scales: (1) fast frequency associated with the longitudinal mode resonances of individual rings (indexed by  $\mu$  and separated by  $\Omega_R$ ) and corresponding fast timescale  $\tau$  in  $[0, \tau_R]$  that

depicts the spatiotemporal field within individual rings; (2) slow frequency ( $\omega_{\text{slow}}$ ) associated with the longitudinal mode resonances of the super-ring resonator (separated by  $\Omega_{\text{SR}}$ ), that is, the frequency response close to a given longitudinal mode resonance of the individual rings and the corresponding slow time  $t \approx 1/J$  that depicts the evolution of fields within the super-ring with round-trip time  $\tau_{\text{SR}}$ . While equations (1) and (3) directly yield the fast-time and fast-frequency response, the Fourier transform of the slow-time ( $t$ ) evolution of  $a_{m,\mu}$  allows us to reconstruct the slow-frequency ( $\omega_{\text{slow}}$ ) spectrum of the topological comb.

For our numerical simulations, we consider a  $12 \times 12$  lattice of site rings and 256 FSRs of individual rings. We use dimensionless parameters<sup>45,46</sup> such that the relevant frequency ( $\omega_{0,\mu}$ ,  $\omega_p$ ,  $\kappa_{\text{ex}}$ ,  $\kappa_{\text{in}}$ ,  $\Omega_R$  and  $D_2$ ) and time ( $\tau_R$  and  $t$ ) scales are normalized by coupling strength  $J$ , and the fields ( $a_{m,\mu}$ ) are normalized by ratio  $\sqrt{J/\gamma}$  (effectively,  $J=1$  and  $\gamma=1$ ; Supplementary Section 2). We chose  $\kappa_{\text{ex}}=0.050$  and  $\kappa_{\text{in}}=0.005$  such that the individual edge state resonances in the edge band are resolved, and  $D_2=0.00025$ .

### Turing rolls and collective coherence

To understand the generation of an optical frequency comb in our topological device, we first fix the (normalized) input pump field at  $\mathcal{E}=1.1$ , and observe the output spectra of the generated photons across multiple FSRs (fast frequency, indexed by  $\mu$ ) as we tune the input pump frequency in one of the FSRs ( $\mu=0$ ; Fig. 2a,b). We find that the generation of the frequency comb (bright light intensity across multiple FSRs) is efficient only when the input pump frequency is close to one of the edge mode resonances. Furthermore, as we will show later, on pumping near the edge mode resonances, the bright frequency comb is generated only in the ring resonators that lie on the edge of the lattice. By contrast, when the input pump frequency is in the bulk bands, the generation of light in FSRs other than the pumped FSR is very weak and the frequency comb is inefficient. This enhanced generation of the optical frequency comb in the edge band is due to the travelling-wave super-ring resonator formed by the edge states that efficiently reinforces the optical frequency comb. The bulk states, on the other hand, do not have a well-defined direction of flow of photons in the lattice (Supplementary Fig. 1).

Having established that the topological optical frequency comb is efficient only when the input pump frequencies excite the edge modes, we now focus on pump frequencies near a single edge mode of the lattice. Figure 2c shows the total pump power ( $\sum_{m \in \text{edge}} |a_{m,\mu=0}|^2$ ) in the super-ring resonator as a function of pump frequency detuning. To reveal the self-formation of temporal features, we plot  $\sum_{m \in \text{edge}} |\tilde{a}_{m,\tau}|^2$  (Fig. 2d), that is, the spatiotemporal (or fast-time  $\tau$ ) intensity distribution integrated over the rings on the edge of the lattice, as a function of the input pump frequency. The presence of sharp features in this plot indicates both self-formation of temporal (or equivalently, spatial) features within individual ring resonators and self-organization of these features across the rings. Randomly varying features in this plot indicate randomness in the spatial intensity distribution within the rings or a lack of coherence between the rings. This plot can be compared with the corresponding plot of a single-ring resonator frequency comb (Fig. 1d and Supplementary Fig. 3).

When the input pump frequency is at  $\delta\omega_{p1} = 0.111J$  in Fig. 2d, we observe a regularly oscillating pattern along the fast-time  $\tau$  axis, which indicates the formation of Turing rolls<sup>5,6</sup> (Supplementary Fig. 3). To confirm this, we plot the spatiotemporal intensity distribution within each ring of the lattice (Fig. 2e), that is,  $|\tilde{a}_{m,\tau}|^2$ , where  $m=(m_x, m_y)$  indicates the location of a ring in the lattice (Supplementary Fig. 1). Indeed, all the rings on the edge of the lattice exhibit equally spaced pulses, called Turing rolls (or perfect soliton crystals)<sup>5,6</sup>. Also, the light intensity in the bulk of the lattice is negligible. Remarkably, we find that the phase of the

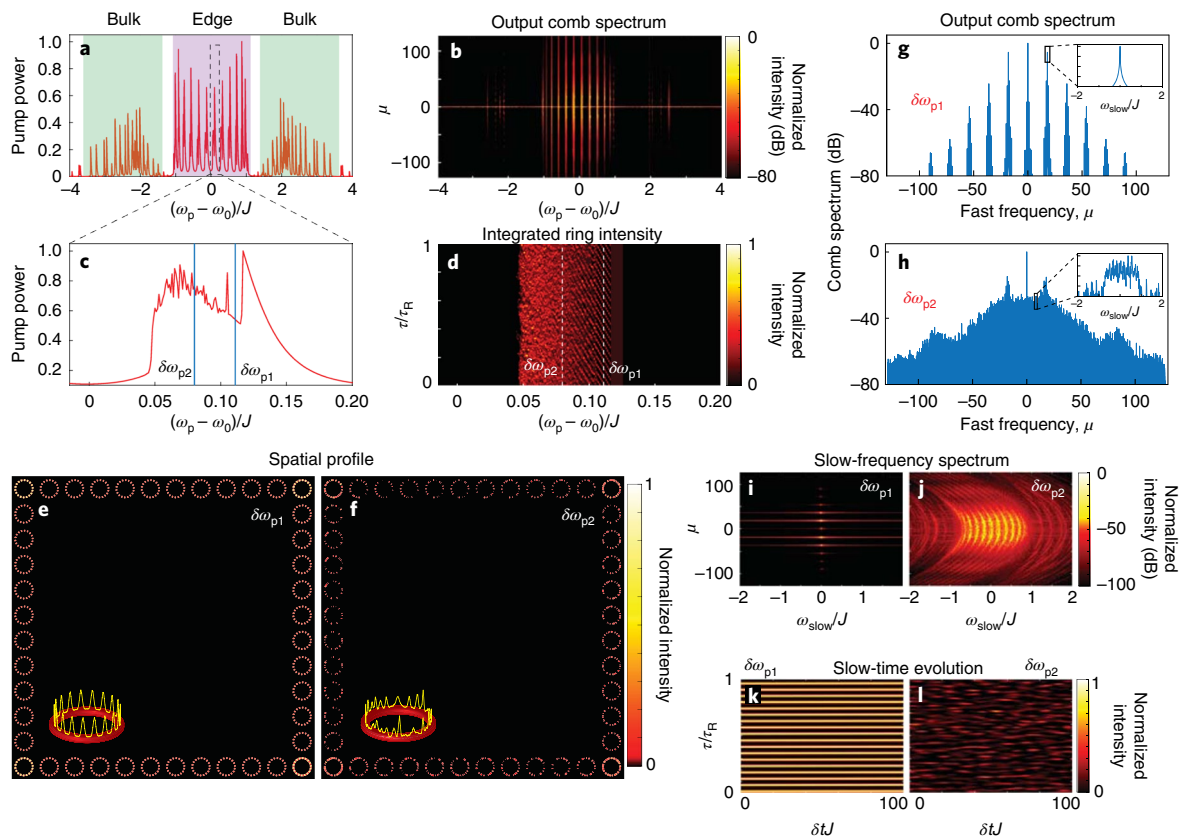


**Fig. 2 | Operation of topological comb in the regimes of Turing rolls and chaos.** **a**, Total pump power in the super-ring resonator as a function of the input pump frequency detuning  $(\omega_p - \omega_0)/J$ , with normalized input pump field  $\varepsilon = 1.1$ . **b**, Spectral power of the generated frequency comb  $(2\kappa_{\text{ex}} |a_{\text{IO},\mu}|^2)$  in different FSRs (indexed by  $\mu$ , the fast frequency). **c**, Total pump power in the super-ring resonator, for pump frequencies in one of the edge state resonances. **d**, Spatiotemporal (or fast-time) intensity distribution in the ring resonators, integrated over the rings on the edge of the lattice  $(\sum_{m \in \text{edge}} |\bar{a}_{m,\tau}|^2)$ , as a function of pump frequency detuning. This plot can be compared with that of a single-ring resonator, as shown in Fig. 1d. We analyse two different pump frequencies, namely,  $\delta\omega_{p1} = 0.111J$  and  $\delta\omega_{p2} = 0.080J$ , as indicated in **c** and **d**. **e-h**, Spatial intensity distribution in the lattice (**e,f**) and output comb spectra (**g,h**) at  $\delta\omega_{p1}$  (**e,g**) and  $\delta\omega_{p2}$  (**f,h**), in the regimes of phase-locked Turing rolls and chaos, respectively. The insets in **e** and **f** show the spatiotemporal intensity distribution in the input-output ring. The insets in **g** and **h** show the slow-frequency spectra for a given longitudinal mode  $\mu$ . For plotting the comb spectra, we chose  $\Omega_R = 20$ . **i-l**, Slow-frequency spectra (**i,j**) and slow-time temporal profiles (**k,l**) at the output for pump frequencies  $\delta\omega_{p1}$  and  $\delta\omega_{p2}$ , respectively.

Turing rolls is locked throughout the edge of the lattice. This shows self-organization or collective spectrotemporal coherence between all the 44 rings on the edge. In fact, there exists a broad region with a bandwidth of  $\sim 0.01J$ , where we observe coherent Turing rolls. From Fig. 2c, we also see that the pump power in the super-ring smoothly varies in this region of coherent Turing rolls (Supplementary Fig. 3).

For lower pump frequencies (near  $\delta\omega_{p2}$  in Fig. 2c,d), we find a chaotic region where the pump power rapidly varies as we tune the input pump frequency. More importantly, the spatiotemporal intensity distribution within each ring, as well as the distribution across rings, is now random without any coherence whatsoever. We emphasize that the pump frequency is still in the edge band, and consequently, the comb intensity is confined to the edge of the lattice and the intensity in the bulk is negligible.

Figure 2g,h shows the output comb spectra for the two pump frequencies  $\delta\omega_{p1}$  and  $\delta\omega_{p2}$ . For  $\delta\omega_{p1}$ , the frequency comb spectrum predominantly consists of discrete spectral lines, separated by 18 FSRs. As in the case of a single-ring frequency comb, this number exactly corresponds to the number of Turing rolls in each ring (Fig. 2e). Furthermore, we have confirmed that the number of Turing rolls decreases as  $\sqrt{\gamma/D_2}$  (refs. 6,45,48) (Supplementary Fig. 4). At  $\delta\omega_{p2}$ , that is, in the chaotic region, the discrete lines in the

primary comb merge together, and there are no distinct features in the frequency spectrum.

Because  $\omega_{\text{slow}} \approx J \ll \Omega_R$ , the slow-frequency spectrum of the comb is not resolved in Fig. 2g,h, which shows the spectra along the fast-frequency axis (FSRs,  $\mu$ ). Therefore, to better visualize the slow-frequency response of the topological comb, we plot the slow-frequency spectrum within each FSR (Fig. 2i,j). Here  $\omega_{\text{slow}}$  ( $x$  axis) is calculated as the detuning from the corresponding longitudinal mode resonance frequency  $\omega_{0,\mu}$  and the input pump frequency, such that  $\omega_{\text{slow}} = \{(\omega_{\mu} - \omega_{0,\mu}) - (\omega_p - \omega_0)\}/J$ , where  $\omega_{\mu}$  is the frequency of generated light in longitudinal mode  $\mu$ .

At  $\delta\omega_{p1}$ , that is, in the region of coherent Turing rolls (Fig. 2i), the slow-frequency spectrum within each bright FSR (fast frequency,  $\mu$ ) exhibits a single mode centred around the comb line (a cross-section of this plot is shown in Fig. 2g, inset). The oscillation of a single edge mode within each oscillating FSR is consistent with the observation of uniform spatial intensity distribution on the edge of the lattice (Fig. 2e). This can also be inferred from Fig. 2k, which shows that the fast-time ( $\tau$ ) intensity distribution at the output remains constant with the evolution of slow time  $t$ .

At  $\delta\omega_{p2}$ , that is, in the chaotic region, we observe the oscillation of multiple modes in the edge band ( $\omega_{\text{slow}} = (-1,1)J$ ) of each FSR.

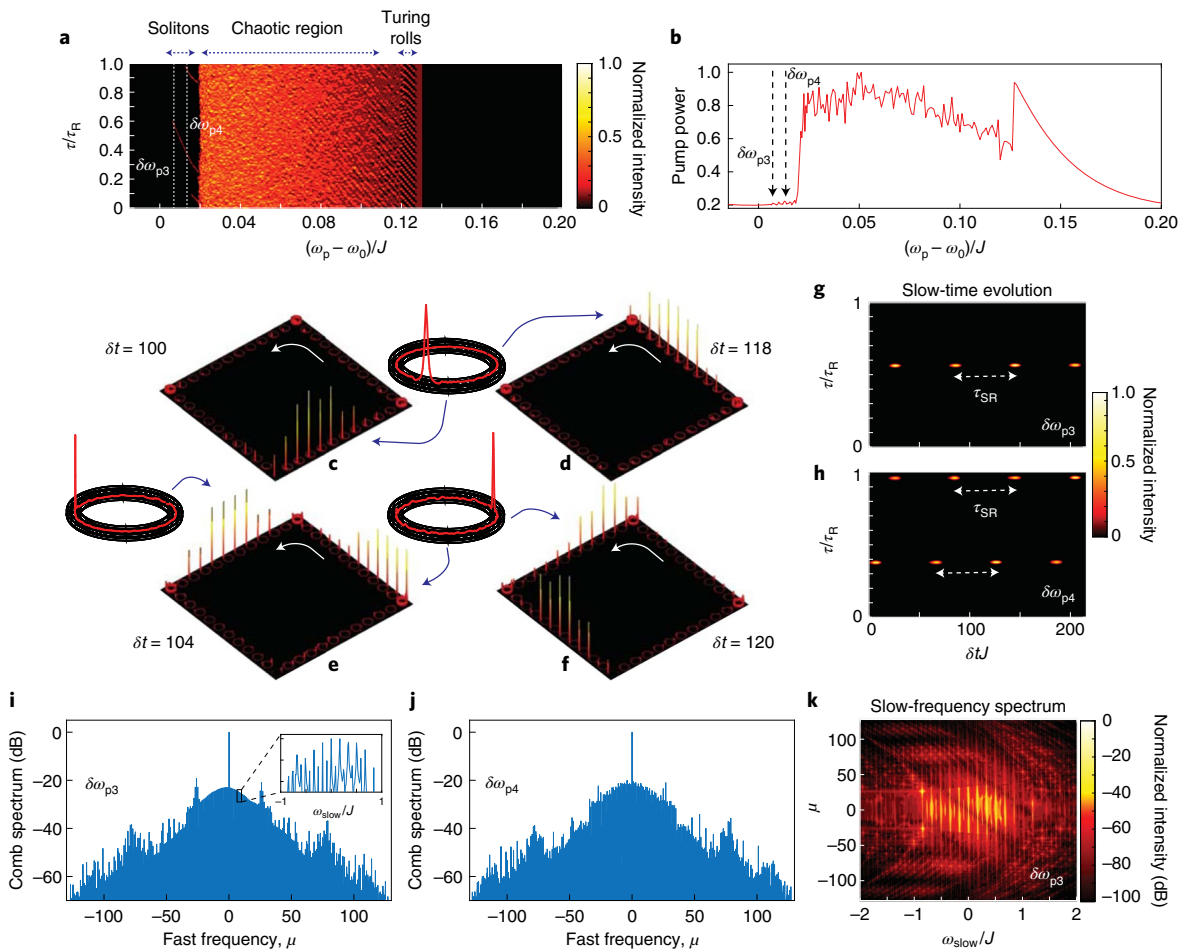


**Fig. 3 | Operation of topological comb in the regime of a nested solitons.** **a**, Spatiotemporal (or fast-time) intensity distribution integrated over edge rings. **b**, Total pump power in the super-ring resonator as a function of the input pump frequency, with input pump field  $\epsilon = 1.56$ . **c, d**, Spatial intensity profiles in the lattice at  $\delta\omega_{p3}$ , for two different slow times,  $\delta t = 100$  (**c**) and  $\delta t = 118$  (**d**), showing the propagation of a single nested soliton (Supplementary Video 1). The inset shows the phase (or position) of the soliton, which is the same for each ring resonator. **e, f**, Propagation of two nested solitons at pump frequency  $\delta\omega_{p4}$ , at two different slow times  $\delta t = 104$  (**e**) and  $\delta t = 120$  (**f**) (also see Supplementary Video 2). The phases of the solitons in individual rings (shown in the insets) are different in the two nested solitons. **g, h**, Temporal profiles at the output for pump frequencies  $\delta\omega_{p3}$  (**g**) and  $\delta\omega_{p4}$  (**h**). **i, j**, Output comb spectra for  $\delta\omega_{p3}$  (**i**) and  $\delta\omega_{p4}$  (**j**). The inset in **i** shows the slow-frequency spectrum (for a given longitudinal mode  $\mu$ ) where multiple equidistant edge modes are oscillating. **k**, Slow-frequency spectrum at  $\delta\omega_{p3}$ , showing the oscillation of individual edge mode resonances with an effectively linear dispersion.

This oscillation of multiple edge modes in the chaotic regime is also evident from the non-uniformity of the spatial intensity distribution in the lattice (Fig. 2f), and the dynamics of the output temporal profile (Fig. 2l) that randomly varies with slow time  $t$ . Furthermore, spectral power in the bulk modes ( $\omega_{\text{slow}} < -1J$  and  $\omega_{\text{slow}} > 1J$ ) is two orders of magnitude smaller compared with those of the edge modes. This validates the observation of negligible light intensity in the bulk of the lattice (Fig. 2f). Note that the oscillating edge modes (Fig. 2j) also show the underlying quadratic dispersion of the ring resonators in different FSRs.

### Temporal Kerr super-solitons

To show the presence of nested solitons in the topological frequency comb, we increase the normalized input pump field to  $\epsilon = 1.56$ . From the spatiotemporal intensity distribution in the super-ring resonator (Fig. 3a), in addition to the coherent Turing rolls and chaotic regions, we observe a new regime ( $0-0.02J$ ) where the light intensity is confined to very narrow regions (thin strands) in the ring resonators. A quick comparison with the analogous spatiotemporal intensity distribution of a single-ring optical frequency comb (Fig. 1d) reveals that this region hosts solitons in the topological frequency

comb. Figure 3b shows the total pump power in the super-ring resonator where—similar to a single-ring comb—we see the emergence of kinks in the region where we expect solitons.

We analyse two different pump frequencies, namely,  $\delta\omega_{p3} = 0.0070J$  and  $\delta\omega_{p4} = 0.0135J$ , in this region, as indicated in Fig. 3. From the spatial intensity distribution (Fig. 3c), we see that at  $\delta\omega_{p3}$ , the topological frequency comb exhibits nested solitons: the intensity distribution along the super-ring resonator (edge) of the lattice is confined to a small region of the edge in the form of a super-soliton, and the intensity distribution within each ring is also confined to a narrow region in the form of a soliton. This nested soliton then circulates along the edge of the lattice in an anticlockwise direction as slow time  $t$  evolves (Supplementary Video 1). Remarkably, the spatiotemporal phase of the solitons in individual rings of the super-soliton is locked (Fig. 3c, inset) as this nested soliton structure circulates around the edge of the lattice. This observation once again highlights the collective coherence or self-organization of multiple nonlinear ring resonators on the edge of the lattice. The corresponding temporal spectrum (Fig. 3g) at the output of the topological frequency comb then shows pulses of light that are separated by  $\tau_{\text{SR}}$ , the round-trip time of the super-ring

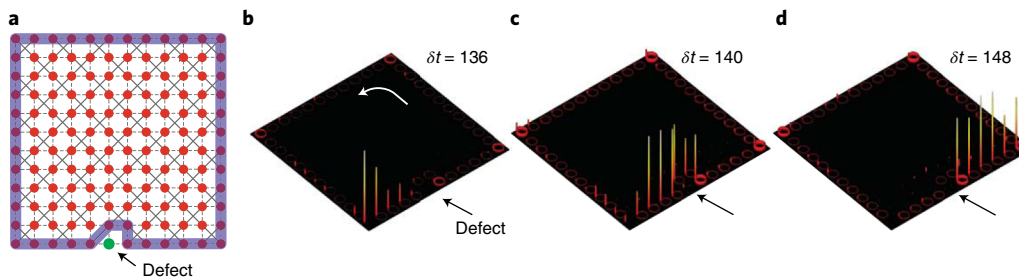


**Fig. 4 | Robustness of the topological comb.** **a**, Schematic of the lattice with a deliberately located defect on the boundary. **b–d**, Robust propagation of a single nested soliton around the defect, at different slow times  $\delta t = 136$  (**b**), 140 (**c**) and 148 (**d**), without any loss of phase-locking or any scattering into the bulk (Supplementary Video 3).

resonator. Note that our simulations are carried out in a reference frame that is rotating at frequency  $\Omega_R/2\pi$ , that is, co-propagating with the solitons in individual rings. Therefore, the solitons in each ring are circulating with time period  $\tau_R$ , and each super-soliton pulse (shown in Fig. 3g) is actually a burst of pulses separated by time  $\tau_R$  (Fig. 1g).

At input pump frequency  $\delta\omega_{p_1}$ , we observe two sets of nested solitons that are simultaneously circulating along the edge of the lattice (Fig. 3e,f and Supplementary Video 2). Furthermore, while the phases of the individual ring solitons within each nested soliton are locked, the corresponding phases in the two nested solitons are not the same (Fig. 3e,f, insets). In contrast to a single nested soliton, the temporal spectrum at the output of the topological frequency comb now consists of two bursts of pulses in each round-trip time  $\tau_{SR}$  of the super-ring resonator. At other pump frequencies in the super-soliton region, we can also observe three nested solitons.

Next, we discuss the frequency spectrum at the output of the topological frequency comb (Fig. 3i,j). In the case of a single nested soliton, that is, at  $\delta\omega_{p_1}$ , the output frequency spectrum is—in general—smooth, which indicates that it is phase-locked (except for few phase jumps; Supplementary Fig. 4). By contrast, in the case of two nested solitons, that is, at  $\delta\omega_{p_2}$ , the frequency spectrum shows small variations (Fig. 3j). This behaviour of the frequency spectra is similar to that observed in single-ring resonator frequency combs where the spectrum is phase-locked only when a single soliton exists in the ring<sup>5,6,45,46</sup>.

Furthermore, by resolving the slow-frequency ( $\omega_{slow}$ ) response of the topological comb (Fig. 3k), we find multiple edge modes that are oscillating within each FSR (Fig. 3i, inset). More importantly, the oscillating edge modes are equally spaced within a given FSR and across FSRs, that is, the intrinsic (linear) dispersion of the longitudinal modes—of both individual ring resonators and super-ring resonator—has now been exactly cancelled by the dispersion induced by the Kerr nonlinearity. Therefore, the frequency spectrum in the regime of a single nested soliton indeed corresponds to that of a coherent nested frequency comb (Fig. 1g). The slow-frequency response also explains the emergence of kinks, as shown in Fig. 3i—these are the regions in which the dispersion curves from two different edge modes interfere and lead to phase jumps in the otherwise coherent frequency comb. This slow-frequency spectrum in the soliton regime can be compared with that of the chaotic regime (Fig. 2j and Supplementary Fig. 5), where multiple modes in the edge band are oscillating but there is no cancellation of dispersion and no phase coherence.

A figure of merit for optical frequency combs operating in the regime of a single soliton is the mode efficiency at the output of the device, that is, the fraction of power that resides in the comb lines other than the pumped mode (Supplementary Section 4). For single-ring resonator optical frequency combs, the mode efficiency in the regime of a single soliton is limited to  $\sim 5\%$ , irrespective of

the length, quality factor or material of the resonator<sup>40–42</sup>. This is because the pulse width of a single soliton is much smaller than the round-trip time of the resonator, which leads to a very small temporal overlap with a CW pump. In comparison, in the regime of a single nested soliton of the topological comb, we observe that 53% of the total output power (in the waveguide) is contained in the comb lines other than the pumped edge mode. This mode efficiency is an order of magnitude higher than that of single-ring resonators and is due to the fact that a single nested soliton pulse (in the super-ring) spans multiple phase-locked ring resonators, with each ring supporting its own single soliton pulse. This enhances the temporal overlap of the nested soliton pulse with the pump. We note that a single-ring comb can also achieve higher efficiency when multiple solitons are present in the ring resonator<sup>5</sup>. However, in this case, the phase (position along the ring) of each soliton pulse is different, and therefore, the comb spectrum is not smooth. In the case of a topological nested soliton, a single ring hosts only a single soliton, and the phase of the solitons across multiple rings is exactly the same, which leads to a smooth spectrum (Fig. 3g). We note that the theoretical limit on the conversion efficiency of the topological nested frequency comb (in the regime of a single nested soliton) could be higher for other parameter regimes.

In the linear regime, the edge states have been demonstrated to be topologically protected against defects in the lattice<sup>18,20,44</sup>. To investigate whether the edge states preserve their robustness in the non-linear regime as well, we explore the propagation of nested solitons in the presence of a deliberately located point defect in the lattice. Specifically, we detune one of the site-ring resonators on the edge of the lattice by  $20J$  (Fig. 4a) such that it is effectively decoupled from the rest of the lattice. Figure 4b–d shows the slow-time evolution of the observed single nested soliton in this lattice (Supplementary Video 3). We see that the nested soliton simply routes around the defect as it circulates along the boundary of the lattice, without losing its phase coherence. We do not observe any light pulses that are reflected from the defect or scattered into the bulk of the lattice. This clearly shows that the nested solitons are indeed topologically robust against defects in the lattice.

## Discussion and outlook

The emergence of coherent temporal features, such as Turing rolls and nested solitons, and the characteristics of a nested frequency comb in the topological super-ring resonator closely resemble those of a single-ring resonator frequency comb in the regime of anomalous dispersion. This allows us to qualitatively depict the phase diagram of the topological frequency comb, as shown in Fig. 5. We perform numerical simulations at different pump powers ( $\epsilon$ ). Using spatiotemporal (fast-time) intensity distributions integrated over the edge rings (similar to Figs. 2d and 3a), we locate the regions of pump frequency detuning that lead to Turing rolls, chaos and nested solitons. In this phase diagram, we have also indicated (upper x axis) the

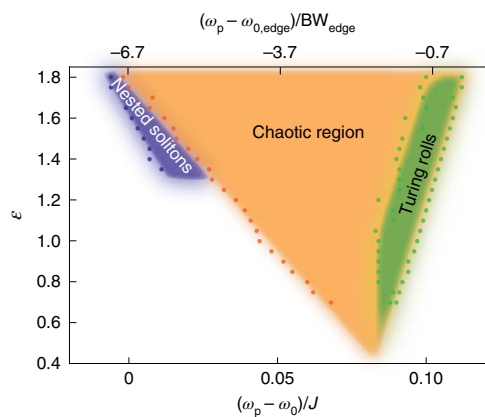


**Fig. 5 | Qualitative phase diagram of the topological frequency comb.** Different operating regimes of the topological comb as a function of the input pump frequency and pump power. The dots indicate the numerical simulation results.

pump frequency detuning from the respective cold-cavity (linear) edge mode resonance ( $\omega_{0,\text{edge}}$ ) and normalized it by its bandwidth ( $\text{BW}_{\text{edge}}$ ). Similar to the case of a single-ring resonator (Fig. 1d and Supplementary Fig. 2), we observe Turing rolls at low pump powers and for pump frequencies near the cold-cavity edge resonance ( $\omega_{0,\text{edge}}$ ). In this regime, the longitudinal modes of the individual rings are phase-locked, which manifests as phase-locking of the Turing rolls across rings. However, only a single mode of the super-ring resonator is excited (Fig. 2g,i). At pump frequencies further away from the cold-cavity edge resonance, we observe a chaotic regime where multiple longitudinal modes of the super-ring resonator are excited in each longitudinal mode of the single rings. But these modes are not phase-locked. Note that in the chaotic regime, the pump frequency and intensity distribution in the lattice still correspond to those of the edge states. This clearly indicates that merely exciting the edge states of the system does not lead to self-organisation or phase-locking. The nested soliton region appears at input pump power  $\varepsilon \approx 1.3$  and at pump frequencies that are far red-detuned from the cold-cavity edge resonance. In this regime, both sets of longitudinal modes (those of single rings and the super-ring) are phase-locked (Supplementary Section 6). This phase-locking is enabled by the unidirectionality and the approximately linear dispersion of the topological edge states (Supplementary Section 8). We observe that the soliton region narrows down, and it completely disappears at higher pump powers, probably leading to another chaotic regime. We note that this qualitative phase diagram was estimated for a given value of dispersion, in one of the edge mode resonances near the centre of the edge band.

While we have shown the presence of many features that are analogous to a single-ring resonator frequency comb, we have only analysed a small subset of parameters that control the topological frequency comb. Therefore, one can expect the appearance of many other known and unknown phases that can emerge from the interaction of edge and bulk modes. It would be intriguing, for example, to explore breathing Turing rolls and nested solitons, dark nested solitons, and platicons in the normal dispersion region<sup>6,46</sup>. In the limit of weak pump powers, our results could pave the way for the generation of quantum optical frequency combs and photonic cluster states entangled in higher dimensions using frequency–time multiplexing<sup>49,50</sup>. Our system could be translated to other frequency regimes of the electromagnetic spectrum, for example, to the microwave domain using circuit quantum electrodynamics platform to implement topological arrays of coupled resonators<sup>51</sup>. One could also explore other topological lattice models to engineer the band

structure and therefore the dispersion of edge and bulk states. In fact, one could go beyond Euclidean geometries and explore the hierarchy of solitons in non-Euclidean curved space, for example, hyperbolic lattices<sup>52</sup>. Therefore, our results open the route to engineer nonlinear parametric processes, spontaneous formation, and self-organization of temporal solitons using synthetic magnetic fields and topological design principles.

### Online content

Any methods, additional references, Nature Research reporting summaries, source data, extended data, supplementary information, acknowledgements, peer review information; details of author contributions and competing interests; and statements of data and code availability are available at <https://doi.org/10.1038/s41567-021-01302-3>.

Received: 4 December 2020; Accepted: 16 June 2021;

Published online: 05 August 2021

### References

- Udem, T., Holzwarth, R. & Hänsch, T. W. Optical frequency metrology. *Nature* **416**, 233–237 (2002).
- Cundiff, S. T. & Ye, J. Colloquium: femtosecond optical frequency combs. *Rev. Mod. Phys.* **75**, 325–342 (2003).
- Diddams, S. A., Vahala, K. & Udem, T. Optical frequency combs: coherently uniting the electromagnetic spectrum. *Science* **369**, eaay3676 (2020).
- Kippenberg, T. J., Holzwarth, R. & Diddams, S. A. Microresonator-based optical frequency combs. *Science* **332**, 555–559 (2011).
- Kippenberg, T. J., Gaeta, A. L., Lipson, M. & Gorodetsky, M. L. Dissipative Kerr solitons in optical microresonators. *Science* **361**, eaan8083 (2018).
- Pasquazi, A. et al. Micro-combs: a novel generation of optical sources. *Phys. Rep.* **729**, 1–81 (2018).
- Gaeta, A. L., Lipson, M. & Kippenberg, T. J. Photonic-chip-based frequency combs. *Nat. Photon.* **13**, 158–169 (2019).
- Del’Haye, P. et al. Optical frequency comb generation from a monolithic microresonator. *Nature* **450**, 1214–1217 (2007).
- Herr, T. et al. Temporal solitons in optical microresonators. *Nat. Photon.* **8**, 145–152 (2013).
- Jang, J. K. et al. Synchronization of coupled optical microresonators. *Nat. Photon.* **12**, 688–693 (2018).
- Tikan, A. et al. Emergent nonlinear phenomena in a driven dissipative photonic dimer. *Nat. Phys.* **17**, 1–7 (2021).
- Helgason, Ó. B. et al. Dissipative solitons in photonic molecules. *Nat. Photon.* **15**, 305–310 (2021).
- Vasco, J. & Savona, V. Slow-light frequency combs and dissipative Kerr solitons in coupled-cavity waveguides. *Phys. Rev. Appl.* **12**, 064065 (2019).
- Lu, L., Joannopoulos, J. D. & Soljačić, M. Topological photonics. *Nat. Photon.* **8**, 821–829 (2014).
- Khanikaev, A. B. & Shvets, G. Two-dimensional topological photonics. *Nat. Photon.* **11**, 763–773 (2017).
- Ozawa, T. et al. Topological photonics. *Rev. Mod. Phys.* **91**, 015006 (2019).
- Hafezi, M., Demler, E. A., Lukin, M. D. & Taylor, J. M. Robust optical delay lines with topological protection. *Nat. Phys.* **7**, 907–912 (2011).
- Hafezi, M., Mittal, S., Fan, J., Migdall, A. & Taylor, J. Imaging topological edge states in silicon photonics. *Nat. Photon.* **7**, 1001–1005 (2013).
- Rechtsman, M. C. et al. Photonic Floquet topological insulators. *Nature* **496**, 196–200 (2013).
- Mittal, S. et al. Topologically robust transport of photons in a synthetic gauge field. *Phys. Rev. Lett.* **113**, 087403 (2014).
- St-Jean, P. et al. Lasing in topological edge states of a one-dimensional lattice. *Nat. Photon.* **11**, 651–656 (2017).
- Bahari, B. et al. Nonreciprocal lasing in topological cavities of arbitrary geometries. *Science* **358**, 636–640 (2017).
- Bandres, M. A. et al. Topological insulator laser: experiments. *Science* **359**, eaar4005 (2018).
- Yang, Z. et al. Mode-locked topological insulator laser utilizing synthetic dimensions. *Phys. Rev. X* **10**, 011059 (2020).
- Cheng, X. et al. Robust reconfigurable electromagnetic pathways within a photonic topological insulator. *Nat. Mater.* **15**, 542–548 (2016).
- Zhao, H. et al. Non-Hermitian topological light steering. *Science* **365**, 1163–1166 (2019).
- Barik, S. et al. A topological quantum optics interface. *Science* **359**, 666–668 (2018).
- Shalaev, M. I., Walasik, W., Tsukernik, A., Xu, Y. & Litchinitser, N. M. Robust topologically protected transport in photonic crystals at telecommunication wavelengths. *Nat. Nanotechnol.* **14**, 31–34 (2019).

29. Gao, X. et al. Dirac-vortex topological cavities. *Nat. Nanotechnol.* **15**, 1012–1018 (2020).
30. Lu, L., Gao, H. & Wang, Z. Topological one-way fiber of second Chern number. *Nat. Commun.* **9**, 5384 (2018).
31. Mittal, S., Goldschmidt, E. A. & Hafezi, M. A topological source of quantum light. *Nature* **561**, 502–506 (2018).
32. Mittal, S., Orre, V. V., Goldschmidt, E. A. & Hafezi, M. Tunable quantum interference using a topological source of indistinguishable photon pairs. *Nat. Photon.* **15**, 542–548 (2021).
33. Blanco-Redondo, A., Bell, B., Oren, D., Eggleton, B. J. & Segev, M. Topological protection of biphoton states. *Science* **362**, 568–571 (2018).
34. Kruk, S. et al. Nonlinear light generation in topological nanostructures. *Nat. Nanotechnol.* **14**, 126–130 (2019).
35. Smirnova, D., Leykam, D., Chong, Y. & Kivshar, Y. Nonlinear topological photonics. *Appl. Phys. Rev.* **7**, 021306 (2020).
36. Lumer, Y., Plotnik, Y., Rechtsman, M. C. & Segev, M. Self-localized states in photonic topological insulators. *Phys. Rev. Lett.* **111**, 243905 (2013).
37. Ablowitz, M. J., Curtis, C. W. & Ma, Y.-P. Linear and nonlinear traveling edge waves in optical honeycomb lattices. *Phys. Rev. A* **90**, 023813 (2014).
38. Leykam, D. & Chong, Y. D. Edge solitons in nonlinear-photonic topological insulators. *Phys. Rev. Lett.* **117**, 143901 (2016).
39. Mukherjee, S. & Rechtsman, M. C. Observation of Floquet solitons in a topological bandgap. *Science* **368**, 856–859 (2020).
40. Xue, X., Wang, P.-H., Xuan, Y., Qi, M. & Weiner, A. M. Microresonator Kerr frequency combs with high conversion efficiency. *Laser Photon. Rev.* **11**, 1600276 (2017).
41. Bao, H. et al. Laser cavity-soliton microcombs. *Nat. Photon.* **13**, 384–389 (2019).
42. Xue, X., Zheng, X. & Zhou, B. Super-efficient temporal solitons in mutually coupled optical cavities. *Nat. Photon.* **13**, 616–622 (2019).
43. Leykam, D., Mittal, S., Hafezi, M. & Chong, Y. D. Reconfigurable topological phases in next-nearest-neighbor coupled resonator lattices. *Phys. Rev. Lett.* **121**, 023901 (2018).
44. Mittal, S., Orre, V. V., Leykam, D., Chong, Y. D. & Hafezi, M. Photonic anomalous quantum Hall effect. *Phys. Rev. Lett.* **123**, 043201 (2019).
45. Chembo, Y. K. & Yu, N. Modal expansion approach to optical-frequency-comb generation with monolithic whispering-gallery-mode resonators. *Phys. Rev. A* **82**, 033801 (2010).
46. Chembo, Y. K. & Menyuk, C. R. Spatiotemporal Lugiato-Lefever formalism for Kerr-comb generation in whispering-gallery-mode resonators. *Phys. Rev. A* **87**, 053852 (2013).
47. Hansson, T., Modotto, D. & Wabnitz, S. On the numerical simulation of Kerr frequency combs using coupled mode equations. *Opt. Commun.* **312**, 134–136 (2014).
48. Godey, C., Balakireva, I. V., Coillet, A. & Chembo, Y. K. Stability analysis of the spatiotemporal Lugiato-Lefever model for Kerr optical frequency combs in the anomalous and normal dispersion regimes. *Phys. Rev. A* **89**, 063814 (2014).
49. Kues, M. et al. On-chip generation of high-dimensional entangled quantum states and their coherent control. *Nature* **546**, 622–626 (2017).
50. Reimer, C. et al. High-dimensional one-way quantum processing implemented on  $d$ -level cluster states. *Nat. Phys.* **15**, 148–153 (2019).
51. Carusotto, I. et al. Photonic materials in circuit quantum electrodynamics. *Nat. Phys.* **16**, 268–279 (2020).
52. Kollár, A. J., Fitzpatrick, M. & Houck, A. A. Hyperbolic lattices in circuit quantum electrodynamics. *Nature* **571**, 45–50 (2019).

**Publisher's note** Springer Nature remains neutral with regard to jurisdictional claims in published maps and institutional affiliations.

© The Author(s), under exclusive licence to Springer Nature Limited 2021

# Supplementary Information: Topological Frequency Combs and Nested Temporal Solitons

Sunil Mittal,<sup>1,2,\*</sup> Gregory Moille,<sup>3,1</sup> Kartik Srinivasan,<sup>3,1</sup> Yanne K. Chembo,<sup>2</sup> and Mohammad Hafezi<sup>1,2,4</sup>

<sup>1</sup>Joint Quantum Institute, NIST/University of Maryland, College Park, MD 20742, USA

<sup>2</sup>Department of Electrical and Computer Engineering, and IREAP,  
University of Maryland, College Park, MD 20742, USA

<sup>3</sup>Microsystems and Nanotechnology Division, Physical Measurement Laboratory,  
National Institute of Standards and Technology, Gaithersburg, MD 20899, USA

<sup>4</sup>Department of Physics, University of Maryland, College Park, MD 20742, USA

## S1. SPECTRUM OF THE LINEAR TOPOLOGICAL RING RESONATOR LATTICE

In this section we discuss the tight-binding description of the topological ring-resonator lattice (shown in Fig.1e of the main text) and its properties in the linear regime. We use a two dimensional square lattice of *site* rings, coupled using *link* rings [1, 2]. The resonance frequencies of the link rings are detuned from those of the site rings by one half free-spectral range (FSR,  $\Omega_R$ ) such that the link rings act as waveguides and introduce a non-zero hopping phase when the photons hop between site rings. [1–4]. Furthermore, near site-ring resonance frequencies, light intensity in the link rings is negligible.

The effective couplings between the site rings are presented in Fig.S1a. While every site ring is coupled to its nearest neighbors (dashed gray lines), next-nearest neighbor couplings (solid gray lines) are present only in alternating plaquettes (a square made of 4 sites, for example, the ones shaded in green or yellow). The hopping phase is zero for the next-nearest neighbor couplings, and is  $\pm\pi/4$  for the nearest neighbor couplings. The direction of nearest-neighbor couplings for which the hopping phase is  $+\pi/4$  is indicated by gray arrows in the inset of Fig.S1a. In this configuration, the lattice simulates the anomalous quantum Hall model for photons with a non-zero local synthetic magnetic flux  $\pi$  threading one half unit cell but a zero magnetic flux through a complete unit cell of the lattice.

The dynamics of the system close to a longitudinal mode resonance (indexed by  $\mu$ ) of the site rings is described by a Haldane-like tight-binding Hamiltonian [1, 2, 5]

$$H_L = \sum_{m,\mu} \omega_{0,\mu} a_{m,\mu}^\dagger a_{m,\mu} - J \sum_{\langle m,n \rangle, \mu} a_{m,\mu}^\dagger a_{n,\mu} e^{-i\phi_{m,n}} - J \sum_{\langle\langle m,n \rangle\rangle, \mu} a_{m,\mu}^\dagger a_{n,\mu} + \text{h.c.} \quad (\text{S1})$$

Here  $a_{m,\mu}$  is the photon annihilation operator at a (site-ring) spatial position  $m = (m_x, m_y)$ , where  $m_x$  and  $m_y$  are the column and row indices, respectively (see Fig.S1a).  $\omega_{0,\mu}$  is the resonance frequency of the site ring resonator longitudinal mode with the integer index  $\mu$ .  $J$  is the coupling strength between ring resonators, and is the same for both nearest (indicated by  $\langle m, n \rangle$ ) and next-nearest neighbor (indicated by  $\langle\langle m, n \rangle\rangle$ ) couplings. Two lattice sites, represented by indices  $m$  and  $n$ , are nearest neighbor coupled along the  $x$ -axis when  $m_x = n_x \pm 1$  and  $m_y = n_y$ , and along the  $y$ -axis when  $m_y = n_y \pm 1$  and  $m_x = n_x$ . The next-nearest neighbor couplings between the two lattice sites requires  $m_x = n_x \pm 1$  and  $m_y = n_y \pm 1$ . As mentioned above, next-nearest neighbor couplings are present only in alternate plaquettes.  $\phi_{m,n} = \pm\frac{\pi}{4}$  is the hopping phase between nearest neighbor sites  $m$  and  $n$ , with its sign as shown in the inset of Fig.S1a. We note that this tight-binding description of our system is valid in the regime  $J \ll \Omega_R$ , and in this linear Hamiltonian the photon operators in different longitudinal modes (indexed by  $\mu$ ) are uncoupled. Moreover, in contrast to the system presented in ref.[1, 2], here the on-site potential is zero, that is, all the site rings have the same resonance frequency.

To probe this lattice, we couple one ring at the corner  $(m_x, m_y) = (1, 1)$  of the lattice to input-output waveguide as shown in Fig.1e of the main text. We refer to this lattice site index as IO (input-output). For an input field  $\mathcal{E}$ , the field at the output of the lattice,  $\mathcal{E}_{\text{out}}$ , is calculated using the input-output formalism as [6, 7]

$$\mathcal{E}_{\text{out}} = \mathcal{E} + i\sqrt{2\kappa_{ex}} a_{\text{IO}}, \quad (\text{S2})$$

where  $\kappa_{ex}$  is the coupling rate of the input-output waveguide to the input-output site ring, and  $|a_{\text{IO}}|^2$  is total energy in the input-output site ring in the give longitudinal mode.

Figure S1b shows the transmission spectrum of a  $12 \times 12$  lattice, near the longitudinal mode  $\mu = 0$  with resonance frequency  $\omega_0$ , as a function of the input light frequency detuning  $(\omega - \omega_0)$ . Because the unit cell of the lattice consists of two lattice sites (see Fig.S1), the frequency spectrum of our topological device exhibits two bulk bands, separated by a bandgap (for an infinite lattice) that hosts edge states [1, 2]. When the input light frequency is in the bulk bands, its spatial intensity distribution in the lattice is spread through the bulk of the lattice (Figs.S1d,h). Furthermore, the photons do not have a well defined momentum or direction of propagation in the lattice (Figs.S1e,i). In contrast, when the input light frequency corresponds to the edge band, its spatial intensity distribution is confined only to the edge of the lattice (Fig.S1f). Moreover, photons in the edge band circulate

around the lattice in counter-clockwise direction, and thereby, realize a travelling-wave super-ring resonator (Fig.S1g). Note that for edge states, the light intensity on the corner rings of the lattice is higher than that on the edge of the lattice because the corners act as defects in the lattice. Nevertheless, because the edge states are topologically protected, the corners can not scatter light backward or into the bulk of the lattice. Figure S1c shows the total power (normalized) in the super-ring resonator formed by edge states. The total power (or energy) in the super-ring resonator is calculated as  $\sum_{m \in edge} |a_m|^2$ . This structure of an edge band sandwiched between two bulk bands repeats in each FSR ( $\Omega_R$ ) of the individual ring resonators.

We also emphasize that our system is time-reversal symmetric and supports a pseudo-spin degree of freedom that corresponds to the circulation direction of photons in the ring resonators [2–4]. Nevertheless, it has been experimentally demonstrated that we can excite a single pseudo-spin in the system, and the parasitic coupling between the two pseudo-spins is negligible such that it effectively breaks time-reversal symmetry for a given pseudo-spin [2, 3, 8]. The edge states corresponding to the two pseudo-spins circulate around the lattice in opposite directions, analogous to the quantum spin-Hall system. The plots shown here show the case when photons circulate clockwise in the site-ring resonators.

## S2. NUMERICAL SIMULATIONS OF THE TOPOLOGICAL FREQUENCY COMB

To generate optical frequency comb in the topological ring resonator array we rely on the intrinsic Kerr nonlinearity of the ring resonators. A continuous-wave (CW) pump laser, with frequency close to one of the longitudinal mode resonances ( $\mu = 0$ ), leads to the generation of photons in other longitudinal modes ( $\mu \neq 0$ ) via four-wave mixing. This nonlinear Kerr interaction is described by the Hamiltonian

$$H_{NL} = -\gamma \sum_{m,\mu} a_{m,\mu_1}^\dagger a_{m,\mu_2}^\dagger a_{m,\mu_3} a_{m,\mu_4} \delta_{\mu_1+\mu_2,\mu_3+\mu_4}, \quad (S3)$$

where two photons at longitudinal modes  $\mu_3$  and  $\mu_4$  annihilate and generate two photons at longitudinal modes  $\mu_1$  and  $\mu_2$ .  $\delta_{\mu_1+\mu_2,\mu_3+\mu_4}$  indicates conservation of energy and momentum in the four-wave mixing interaction, and  $\gamma$  is the strength of nonlinear interaction. Note that the nonlinear Kerr interaction is local to a ring resonator, and therefore, couples multiple super-ring (edge state) resonances.

To simulate our topological frequency comb we use the linear and nonlinear tight-binding Hamiltonians of Eqs.S1,S3 and derive the coupled Lugiato-Lefever equations (LLEs) [9–11] that describe the dynamics of the topological frequency comb as

$$\begin{aligned} \frac{da_{m,\mu}}{dt} = & -i(\omega_{0,\mu} - \Omega_R \mu - \omega_p) a_{m,\mu} - J \sum_{\langle n \rangle} a_{n,\mu} e^{-i\phi_{m,n}} - J \sum_{\langle\langle n \rangle\rangle} a_{n,\mu} \\ & + i\gamma \frac{1}{\tau_R} \int_0^{\tau_R} d\tau \left( |\tilde{a}_{m,\tau}|^2 \tilde{a}_{m,\tau} \right) e^{-i\omega_{0,\mu}\tau} - (\kappa_{ex} \delta_{m,10} + \kappa_{in}) a_{m,\mu} + \delta_{m,10} \delta_{\mu,0} \sqrt{2\kappa_{ex}} \mathcal{E}. \end{aligned} \quad (S4)$$

For our numerical simulations, we rewrite this equation using dimensionless parameters. We multiply both sides of the equation by  $\sqrt{\gamma/J^3}$ , and redefine dimensionless parameters as

$$\begin{aligned} \frac{\omega_{0,\mu}}{J} \rightarrow \omega_{0,\mu} \quad \frac{\omega_p}{J} \rightarrow \omega_p \quad \frac{\Omega_R}{J} \rightarrow \Omega_R \quad \frac{\kappa_{ex}}{J} \rightarrow \kappa_{ex} \quad \frac{\kappa_{in}}{J} \rightarrow \kappa_{in} \\ Jt \rightarrow t \quad J\tau_R \rightarrow \tau_R \quad \sqrt{\frac{\gamma}{J}} a \rightarrow a \quad \sqrt{\frac{2\kappa_{ex}\gamma}{J^3}} \mathcal{E} \rightarrow \mathcal{E}. \end{aligned} \quad (S5)$$

We consider a pump field  $\mathcal{E}$  injected into the lattice in the longitudinal mode  $\mu = 0$ , and the resulting fields  $\mathcal{E}_{out,\mu}$  at the output of the frequency comb are calculated using the input-output formalism as

$$\mathcal{E}_{out,\mu} = \mathcal{E} \delta_{\mu,0} + i\sqrt{2\kappa_{ex}} a_{10,\mu}. \quad (S6)$$

The output comb spectrum in different longitudinal modes (the fast frequency) is then calculated as  $|\mathcal{E}_{out,\mu}|^2$ .

In our simulations we scan the pump frequency  $\omega_p$  from higher ( $0.2J$  in Fig. 2 and 3 of the main text) to lower frequencies ( $-0.05J$ ), in steps of  $0.001J$  in the region of Turing rolls and chaos, and in steps of  $0.0005J$  in the region of nested solitons. For each pump frequency, we perform 8192 iterations using the fourth-order Runge-Kutta method and the split-step protocol [9], with a fixed time step of  $0.1/J$  (corresponds to the slow time  $t$ ). We use the final state ( $a_{m,\mu}$ ) calculated for each pump frequency as initial state for the successive pump frequency. The initial state for first pump frequency is chosen to be of random amplitudes and phases (both across the rings and across longitudinal modes). We find that the results are largely independent of the initial conditions. In Fig.S2 we show simulation results for five consecutive runs with different initial conditions (random).

The first column shows the fast-time response integrated over the super-ring resonator, the second column shows the total pump power in the super-ring, and the last column shows spatial intensity profile in the lattice for a fixed pump frequency  $0.007J$  (same as in the main text). In all cases, we observe phase-locked nested solitons, although the phase of the solitons and exact dynamics of solitons, like the number of nested solitons, vary from run to run, as is also the case for single ring frequency combs.

To calculate the slow frequency response of the frequency comb near each longitudinal mode  $\mu$ , we let the fields ( $a_{m,\mu}$ ) stabilize for 8192 iterations. We then Fourier transform the next 8192 iterations (with fixed time steps of  $0.1/J$ ) of the field in the input-output ring  $a_{IO,\mu}(t)$  to get  $a_{IO,\mu}(\omega_{slow})$ . The frequency comb spectrum in the output waveguide is then calculated using the input-output formalism as discussed above. Note that for longitudinal modes other than the pumped mode, the output comb power is simply  $2\kappa_{ex}|a_{IO,\mu}(\omega_{slow})|^2$ . The temporal field distribution within a ring (fast-time scale) is calculated using Fourier transform over the 256 longitudinal modes (indexed by  $\mu$ , see Eq. 3 of the main text).

The mode efficiency of the frequency comb is calculated as

$$\frac{\sum_{\substack{\mu, \mu \neq 0 \\ \omega_{slow}}} |\mathcal{E}_{out,\mu}(\omega_{slow})|^2}{\sum_{\omega_{slow}^{\mu}} |\mathcal{E}_{out,\mu}(\omega_{slow})|^2}, \quad (S7)$$

where  $\mathcal{E}_{out,\mu}(\omega_{slow})$  is the field in the output waveguide at longitudinal mode  $\mu$  and slow-frequency  $\omega_{slow}$ . Therefore, the denominator is the total power in the comb, and the numerator is the total power in generated comb lines, that is, excluding the pumped mode ( $\mu = 0, \omega_{slow} = 0$ ).

### S3. EXPERIMENTAL REALIZATION OF THE TOPOLOGICAL FREQUENCY COMB

From an experimental perspective, our topological coupled ring resonator design has already been implemented on silicon-on-insulator platform [2], and has been used to generate spectrally engineered energy-time entangled photon pairs via spontaneous-four wave mixing [12, 13]. Some of the parameters used in our simulation, such as the (field) coupling rates  $J/2\pi$  and  $\kappa_{ex}/2\pi = 0.05J/2\pi$ , can be tuned easily, to say,  $2.5 \times 10^9 \text{ s}^{-1}$ , and  $125 \times 10^6 \text{ s}^{-1}$ , respectively. The required loss rate  $\kappa_{in}/2\pi = 0.005J/2\pi = 12.5 \times 10^6 \text{ s}^{-1}$  (intrinsic quality factor of  $\approx 8 \times 10^6$  at telecom wavelengths) can also be achieved on ultra low-loss silicon-nitride platform [11, 14]. For the results presented in the main text we choose the dispersion parameter  $D_2/2\pi = 0.00025J/2\pi = 0.625 \text{ MHz}$ , but as we show in Section S5 of the Supplementary Information, it can vary over a wide range.

For example, the ring waveguides could be 800 nm high and  $1 \mu\text{m}$  wide, with total ring length ( $L$ ) of  $\sim 100 \mu\text{m}$  and corresponding FSR ( $\Omega_R/2\pi$ ) of  $\sim 1400 \text{ GHz}$  (with  $N_g \sim 2.12$ ). The coupling strengths  $J/(2\pi) = 2.5 \times 10^9 \text{ s}^{-1}$  and  $\kappa_{ex}/(2\pi) = 125 \times 10^6 \text{ s}^{-1}$  can be achieved with coupling gaps in the range of 200-800 nm, which are also accessible using the deep-UV projection photolithography.

From numerical simulations presented in Fig. 3 of the main text, we see that the normalized pump field  $\mathcal{E}$  required to observe nested solitons is  $\sim 1.56$ . The corresponding actual pump power would then be  $|\mathcal{E}|^2 J^3 / (2\kappa_{ex}\gamma) \sim 16 \text{ W}$ , assuming  $\gamma = c\omega_0 n_2 / n_0^2 A_{eff} L \sim 3.7 \times 10^{20} \text{ W}^{-1} \text{ s}^{-2}$ . We note that this definition of  $\gamma$  is different from that found in the literature where it is defined as  $\omega_0 n_2 / c A_{eff}$ .

A major consideration in the experimental realization of our design is the intrinsic fabrication-induced disorder in the ring resonance frequencies, coupling strengths, and hopping phases. While here we have shown the robustness of topological Kerr super-solitons only against discrete defects in the lattice, our topological ring resonator design has been experimentally demonstrated to be robust against such random disorders that exist in practical systems [8, 13]. Nevertheless, the strength of disorder sets a lower bound on the coupling strength  $J$  because the edge states in our design are robust as long as the disorder strength is less than the width of the topological bandgap ( $\sim 2J$ ) [8, 13]. The choice  $J/2\pi = 2.5 \times 10^9 \text{ s}^{-1}$  fulfills this criteria as the disorder strength  $U/2\pi \sim 5 \text{ GHz}$  in state-of-the-art photonic ring resonators. However, an increase in the disorder strength, and thereby, the coupling strength  $J$ , will increase the pump power required to access the nested soliton regime, and subsequently, may lead to undesirable thermal effects in the system. Nonetheless, because the pump power is distributed across all the ( $> 40$ ) rings on the edge of the lattice, we do not expect the thermal effects to be a bigger issue than it is for single-ring combs. Moreover, thermal effects do not affect the existence of the soliton solutions; they impact experimental access to the soliton regime when tuning pump power and frequency. A variety of techniques (for example, power kicking, fast frequency ramps, auxiliary pumping, etc.) could be used to overcome the thermal effects and access the nested soliton regime, as is usually done for single-ring combs. Furthermore, we note that for a given ratio  $J/\kappa_{ex}$ , the pump power scales as  $J^2$ . Therefore, even small improvements in the strength of disorder, say by a factor of 2, will reduce the required pump power by a factor of 4. Reducing dispersion of the ring resonators and optimizing the ratio  $J/\kappa_{ex}$  can lead to a further reduction in the required pump power. Therefore, we believe our topological frequency comb design can be implemented using existing integrated photonic platforms and state-of-the-art nanofabrication technology.

#### S4. OPTICAL FREQUENCY COMB AND DISSIPATIVE KERR-SOLITONS IN A SINGLE RING RESONATOR

In this section we discuss the generation of an optical frequency comb, and temporal features such as Turing rolls and Kerr solitons in a single ring resonator, in an all-pass filter geometry (Fig. 1a of the main text). This discussion serves to highlight the similarities between a single-ring resonator frequency comb and our topological frequency comb that uses super-ring resonator formed by the edge states.

Fig.S3a shows the the normalized pump power in the ring as a function of the normalized input pump frequency detuning  $\delta\omega_p = (\omega_p - \omega_0) / (\kappa_{ex} + \kappa_{in})$ . Here  $\omega_0$  is the cold cavity resonance in the pump FSR, and  $\kappa_{ex}$  and  $\kappa_{in}$  are the coupling and loss rates respectively.  $(\kappa_{ex} + \kappa_{in})$  is the bandwidth of the all-pass filter in the linear regime. This spectrum was calculated using the Lugiato-Lefever formalism [10, 11, 14]. Fig.S3b shows the corresponding temporal intensity distribution in the ring as a function of fast-time  $\tau/\tau_R$ . Because the Lugiato-Lefever formalism uses a frame that is rotating at  $\Omega_R = 2\pi/\tau_R$ , the round-trip time of the ring, the temporal intensity distribution is synonymous with the spatial intensity distribution in the ring.

We analyze three input pump frequencies in three different regions, as indicated in Figs.S3a,b. At  $\delta\omega_{p1} = -0.125$ , we observe the formation of Turing rolls in the rings (Fig.S3c). The corresponding frequency comb spectrum, in Fig.S3d, shows the presence of only a discrete set of longitudinal modes, separated by 12 FSRs. This frequency spacing (12) also corresponds to the number of Turing rolls in the ring resonator. Furthermore, the region of Turing rolls appears near  $\delta\omega_p = 0$ , and the pump spectrum in this region shows a smooth behaviour. These plots can be compared with Figs.2c,d,e,g of the main text which show similar Turing rolls that are phase-locked across each ring on the edge of the lattice, a similar frequency comb spectrum, and similar smoothly varying pump spectrum in the region of Turing rolls.

At around  $\delta\omega_{p2} = -2.5$ , we observe a chaotic region where the pump spectrum varies rapidly as a function of pump frequency. In this region, the spatial intensity profile in the ring is chaotic and does not show any distinct features (Figs.S3e). Furthermore, this is not a stationary solution meaning that the profile changes with slow-time evolution. The corresponding frequency comb, in Fig. S3f, also shows random variations, but in contrast to Turing rolls, all the longitudinal modes are oscillating (Figs.S3f). These plots can be compared with those of Fig.2f,h,i of the main text where we see a random spatial intensity distribution which varies from ring to ring, and non-stationary solutions at the output.

At around  $\delta\omega_{p3} = -5$ , the pump spectrum shows step-like features. In this region we observe a single soliton in the ring resonator (Figs.S3g), with a frequency comb spectrum that is coherent and smooth across FSRs (Figs.S3h). This is a stationary solution meaning that the intensity profile in the ring does not change with slow-time evolution. These plots can be compared with plots in Fig.3a-d of the main text where we observe similar step-like features in the pump spectrum, and a nested soliton which is further made of phase-locked solitons in the individual ring resonators.

We note that single-soliton pulse width is much smaller than the round trip time in the ring resonator. Therefore, the temporal overlap between the single-soliton pulse and the continuous-wave pump is small [15], leading to a low mode efficiency of  $\sim 4\%$ . In the regime of Turing rolls (also called perfect soliton crystals), the presence of multiple pulses in the ring leads to a better temporal overlap, and therefore, better mode efficiency of  $\sim 13\%$ . In contrast, the mode efficiency in the chaotic regime is much higher  $\sim 55\%$  because there are no discrete pulses in the ring, and therefore, the temporal mode overlap with the continuous-wave pump is significant. Furthermore, optical frequency combs implemented using two coupled cavities, one for recycling the pump and the other for generating the solitons, have also been shown to achieve an efficiency of 75% [15, 16] or more in the regime of single solitons. However, these configurations require two cavities with disparate lengths, for example, a ring resonator and a fiber loop, and are therefore, challenging to integrate on a photonic chip.

#### S5. NUMBER OF TURING ROLLS AS A FUNCTION OF DISPERSION

For a single ring resonator frequency comb in the anomalous dispersion regime, the number of Turing rolls  $N_{\text{Rolls}}$  decreases with increasing dispersion as  $\sqrt{\gamma/D_2}$ , where  $D_2$  is the second-order dispersion coefficient [9, 10], and  $\gamma$  is the nonlinear coefficient which, in the Lugiato-Lefever formalism, is effectively normalized to 1 (see Section 2). We observe identical behaviour in our topological frequency comb. In Fig.S4a we plot the number of Turing rolls in the topological frequency comb as we vary the dispersion parameter  $D_2$ , for a fixed input pump field  $\mathcal{E} = 1.1$ . A fit (solid-line) to the numerically simulated data (open circles), shows that indeed  $N_{\text{Rolls}} \propto 1/\sqrt{D_2}$ .

To show self-organization of the ring resonators on the edge of the lattice across a range of dispersion values, in Figs.S4b,c we plot the integrated spatio-temporal intensity distributions (integrated over the super-ring resonator) as a function of the input pump frequency, for  $D_2 = 0.0014$  and  $D_2 = 0.0025$ , respectively. Figs.S4d,e show complete spatial intensity distributions in the lattice when the input pump frequency is in the region of Turing rolls ( $\omega_p - \omega_0 = 0.1J$ ). Similar to Fig.2 of the main text, we observe that the Turing rolls in all the ring resonators on the edge are locked to the same spatio-temporal phase. Similarly, we also observe the presence of nested solitons. Note that the dispersion values used here are 5-10 times of that used in Fig.2 and Fig.3 of the main text.

## S6. PHASE COHERENCE OF THE SUPER-SOLITON FREQUENCY COMB

In this section we show the phase coherence of our topological frequency comb in the regime of super-solitons. Figure S5a shows the integrated pump power in the super-ring resonator at  $\mathcal{E} = 1.56$  (same as Fig.3a of the main text, repeated here for convenience). Figures S5b,g show the output frequency spectrum (both slow and fast frequencies) of the comb at pump frequencies  $\delta\omega_{p3} = 0.007J$  in the single nested soliton region, and at  $\delta\omega_{p5} = 0.10J$  in the chaotic region. As we discussed in the main text, the comb spectrum in the nested soliton regime (Fig.S5b) shows oscillations of multiple equidistant edge modes with in a single FSR ( $\mu$ ) of the individual ring resonators. Furthermore, we observe cancellation of linear dispersion by nonlinearity-induced dispersion across multiple single ring FSRs (indexed by  $\mu$ , the fast frequency). In contrast, the comb spectrum in the chaotic region (Fig.S4g) also shows oscillation of multiple modes, but no cancellation of dispersion.

In a single-ring frequency comb, in the single soliton regime, cancellation of dispersion leads to phase coherence such that the output power varies smoothly across the comb lines [9–11, 14]. To show that our topological frequency comb is also phase coherent in the regime of single nested soliton, in Figs.S5c-f we plot the spectral power and the phase of two oscillating edge modes resonances (at  $\omega_{slow} = 0, 0.17J$ ) along the fast-frequency axis. The spectral power indeed varies smoothly across the comb lines in a region  $-31 < \mu < 31$ . However, near  $\mu \approx \pm 32$  and  $\pm 50$ , and more frequently at higher  $\mu$ , we observe jumps in the comb spectrum. From Fig.S5b, we see that these jumps in the spectrum appears when two edge modes interfere because of residual dispersion (the start-like patterns in Fig.S5b).

The corresponding phase (Fig.S5d,f) of the comb lines in the nested soliton region also varies linearly in the regime  $-31 < \mu < 31$  which shows that our comb is indeed phase-coherent. Nevertheless, we observe phase jumps exactly at locations of jumps in the comb spectrum (dashed red-lines in Fig.S5e,f). Within regions between two jumps, the phase variation is again linear. In contrast, the frequency comb in the chaotic region (Fig.S5h-k) exhibits randomly varying power and phase across the comb lines, indicating that the comb is not coherent. Note that here we have plotted the unwrapped phase to explicitly show its linear profile.

## S7. PUMPING ANOTHER EDGE STATE RESONANCE

In the main text, we presented results for pumping one of the edge state resonances in the middle of the edge band ( $\approx [0, 0.2] J$ ). Fig.S6 shows simulation results for pumping another edge state resonance, in the range  $\approx [-0.25, -0.05] J$  (indicated by dashed rectangle in Fig.S6a). Figure S6b shows the total pump power in the super-ring resonator for this edge band, and Fig.S6c shows the spatio-temporal (fast time) intensity distribution in the ring resonators, integrated over all the rings in the super-ring resonator. These plots are very similar to those shown in Fig.2 and Fig.3 of the main text. As before, the spatial intensity distribution shows a region of Turing rolls that are phase-locked through out the rings on the edge of the lattice, and a region of nested solitons. Fig.S6d shows a single nested soliton at pump frequency indicated by dashed lines in Figs.S6b,c. Here, we chose  $D_2 = 0.001$ , and  $\mathcal{E} = 1.47$ .

## S8. DISPERSION OF EDGE STATES

In our numerical simulations, we include second-order anomalous dispersion  $D_2$  for the ring resonance frequencies  $\omega_{0,\mu}$ . As we mentioned in the main text, the dispersion of the edge states resonances (longitudinal modes of the super-ring resonator) within a single FSR of the individual ring resonators is completely determined by the tight-binding Hamiltonian of Eq.S1. Figure S7a shows the energy eigenvalues for this Hamiltonian, calculated for a  $12 \times 12$  lattice of ring (site) resonators. Figure S7b shows a zoom-in of the eigenvalues in the edge band ( $\approx (-1, +1) J$ ). While the edge states in the center of the edge band can be well described by a linear dispersion, as is usually accepted in the condensed-matter community, we see that the edge state resonances closer to the bulk bands do exhibit significant nonlinear dispersion.

We use a third-order polynomial to fit the edge state resonances (shown in Fig.S7b as solid-line) such that  $\omega_{0,\nu} = \omega_{0,\nu_0} + \Omega_{SR}(\nu - \nu_0) + \frac{D_2^{edge}}{2}(\nu - \nu_0)^2 + \frac{D_3^{edge}}{6}(\nu - \nu_0)^3$ . Here  $\omega_{0,\nu}$  are the edge state resonance frequencies indexed by  $\nu$ ,  $\nu_0$  is the resonance in the center of the edge band (here 72nd eigenvalue),  $D_2^{edge}$  and  $D_3^{edge}$  are the second- and third-order dispersion coefficients, respectively. For the  $12 \times 12$  lattice, we find  $\Omega_{SR} = 0.2328J$ ,  $D_2^{edge} = -0.0062J$ , and  $D_3^{edge} = -0.0123J$ . Figure S7c shows integrated dispersion that is  $\frac{D_2^{edge}}{2}(\nu - \nu_0)^2 + \frac{D_3^{edge}}{6}(\nu - \nu_0)^3$ . Therefore, we find that the dispersion of the edge states is in fact dominated by the third-order dispersion  $D_3^{edge}$ . Furthermore,  $D_2^{edge}/\Omega_{SR} \simeq -26 \times 10^{-3}$ , and  $D_3^{edge}/\Omega_{SR} \simeq -53 \times 10^{-3}$ .

Figures S7d-f show corresponding results for a  $60 \times 60$  lattice. In this case, we find  $\Omega_{SR} = 0.0508J$ ,  $D_2^{edge} = -5.938 \times$

$10^{-5} J$ , and  $D_3^{edge} = -11.598 \times 10^{-5} J$ . Note that the ratios  $D_2^{edge}/\Omega_{SR} \simeq -1.2 \times 10^{-3}$ , and  $D_3^{edge}/\Omega_{SR} \simeq -2.3 \times 10^{-3}$ . These are an order of magnitude smaller compared to that of the  $12 \times 12$  lattice, suggesting that the effective nonlinear dispersion of the edge states decreases with increasing lattice size. This is because edge state resonances in the center of the edge band exhibit linear dispersion, and the nonlinear dispersion originates only from regions closer to the bulk bands. With increasing lattice size, the relative contribution of the regions closer to the bulk bands decreases. Note that the width of the edge band is  $\simeq 2J$ , irrespective of the size of the lattice.

---

\* Email: mittals@umd.edu

- [1] Leykam, D., Mittal, S., Hafezi, M. & Chong, Y. D. Reconfigurable topological phases in next-nearest-neighbor coupled resonator lattices. *Phys. Rev. Lett.* **121**, 023901 (2018).
- [2] Mittal, S., Orre, V. V., Leykam, D., Chong, Y. D. & Hafezi, M. Photonic anomalous quantum hall effect. *Phys. Rev. Lett.* **123**, 043201 (2019).
- [3] Hafezi, M., Mittal, S., Fan, J., Migdall, A. & Taylor, J. Imaging topological edge states in silicon photonics. *Nature Photonics* **7**, 1001 (2013).
- [4] Hafezi, M., Demler, E. A., Lukin, M. D. & Taylor, J. M. Robust optical delay lines with topological protection. *Nature Physics* **7**, 907 (2011).
- [5] Haldane, F. D. M. Model for a quantum hall effect without landau levels: Condensed-matter realization of the "parity anomaly". *Phys. Rev. Lett.* **61**, 2015–2018 (1988).
- [6] Gardiner, C. W. & Collett, M. J. Input and output in damped quantum systems: Quantum stochastic differential equations and the master equation. *Phys. Rev. A* **31**, 3761–3774 (1985).
- [7] Little, B. E., Chu, S. T., Haus, H. A., Foresi, J. & Laine, J. . Microring resonator channel dropping filters. *Journal of Lightwave Technology* **15**, 998–1005 (1997).
- [8] Mittal, S. *et al.* Topologically robust transport of photons in a synthetic gauge field. *Phys. Rev. Lett.* **113**, 087403 (2014).
- [9] Chembo, Y. K. & Yu, N. Modal expansion approach to optical-frequency-comb generation with monolithic whispering-gallery-mode resonators. *Phys. Rev. A* **82**, 033801 (2010).
- [10] Chembo, Y. K. & Menyuk, C. R. Spatiotemporal lugiato-lefever formalism for kerr-comb generation in whispering-gallery-mode resonators. *Phys. Rev. A* **87**, 053852 (2013).
- [11] Pasquazi, A. *et al.* Micro-combs: A novel generation of optical sources. *Phys. Rep.* **729**, 1–81 (2018).
- [12] Mittal, S., Orre, V. V., Goldschmidt, E. A. & Hafezi, M. Tunable quantum interference using a topological source of indistinguishable photon pairs. *Nat. Photonics* (2021).
- [13] Mittal, S., Goldschmidt, E. A. & Hafezi, M. A topological source of quantum light. *Nature* **561**, 502 (2018).
- [14] Kippenberg, T. J., Gaeta, A. L., Lipson, M. & Gorodetsky, M. L. Dissipative kerr solitons in optical microresonators. *Science* **361** (2018).
- [15] Xue, X., Zheng, X. & Zhou, B. Super-efficient temporal solitons in mutually coupled optical cavities. *Nat. Photonics* **13**, 616–622 (2019).
- [16] Bao, H. *et al.* Laser cavity-soliton microcombs. *Nat. Photonics* **13**, 384–389 (2019).

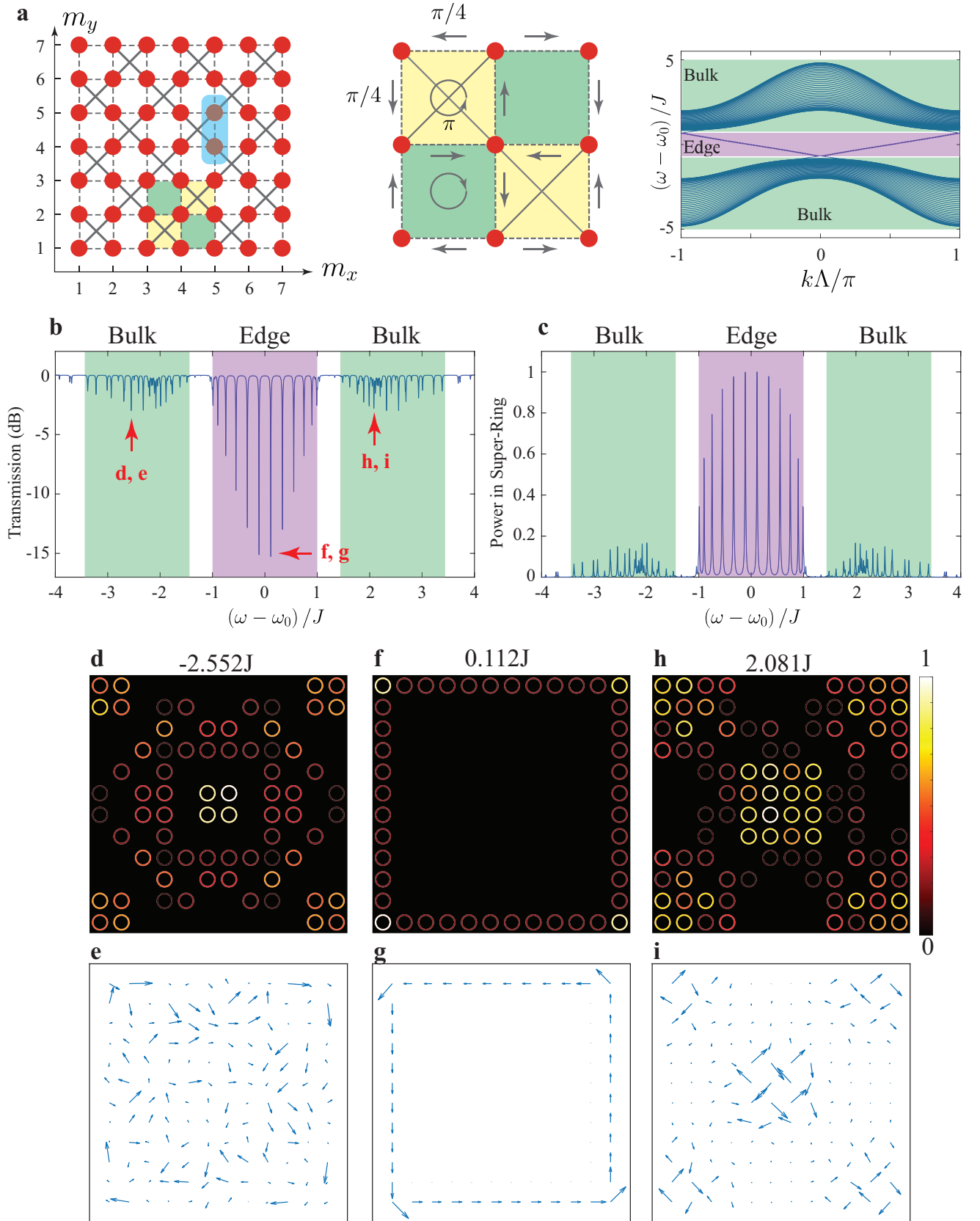


FIG. S1. **a** Effective tight-binding model of the lattice and indexing scheme for a lattice of size  $6 \times 6$ . A unit cell of the lattice, consisting of two sites, is shaded in light blue. The insets show hopping phases within a plaquette, and the band structure of a semi-infinite lattice (finite along one axis, periodic boundary conditions along the other) [2]. Here  $k\Lambda$  is the phase between neighboring unit cells along the axis with periodic boundary conditions. **b** Linear transmission spectrum for a  $12 \times 12$  lattice, and **c** total power (normalized) in the super-ring resonator formed by rings on the edge of the lattice. The edge and the bulk bands are highlighted in purple and green, respectively. Spatial intensity distribution, and the direction of flow of photons in the lattice when the input light frequency is, **d, e** in the left bulk band, at  $\omega - \omega_0 = -2.552J$ , **f, g** in the edge band, at  $\omega - \omega_0 = 0.112J$ , and **h, i** in the right bulk band, at  $\omega - \omega_0 = 2.081J$ . The peaks in the edge band of Fig.S1**b, c** are the longitudinal modes of this super-ring resonator. The plots here show only the site ring resonators.

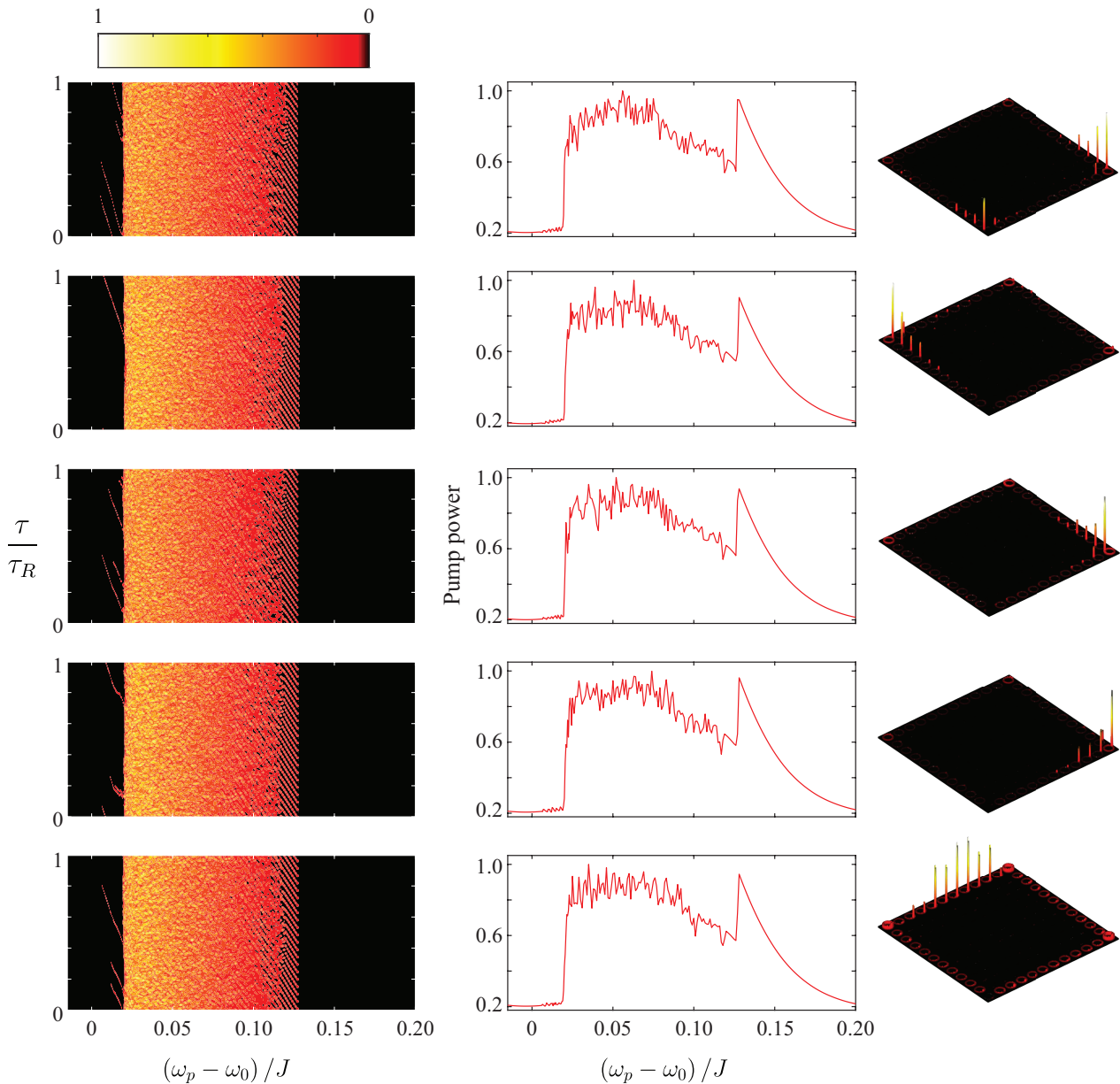


FIG. S2. Numerical simulation results for 5 consecutive runs with different, random initial conditions. The first column shows the fast-time response integrated over the super-ring resonator, the second column shows the total pump power in the super-ring, and the last column shows spatial intensity profile in the lattice for a fixed pump frequency  $0.007J$  (same as in the main text). We observe nested solitons in all cases, though as expected, their exact dynamics does vary with initial conditions.

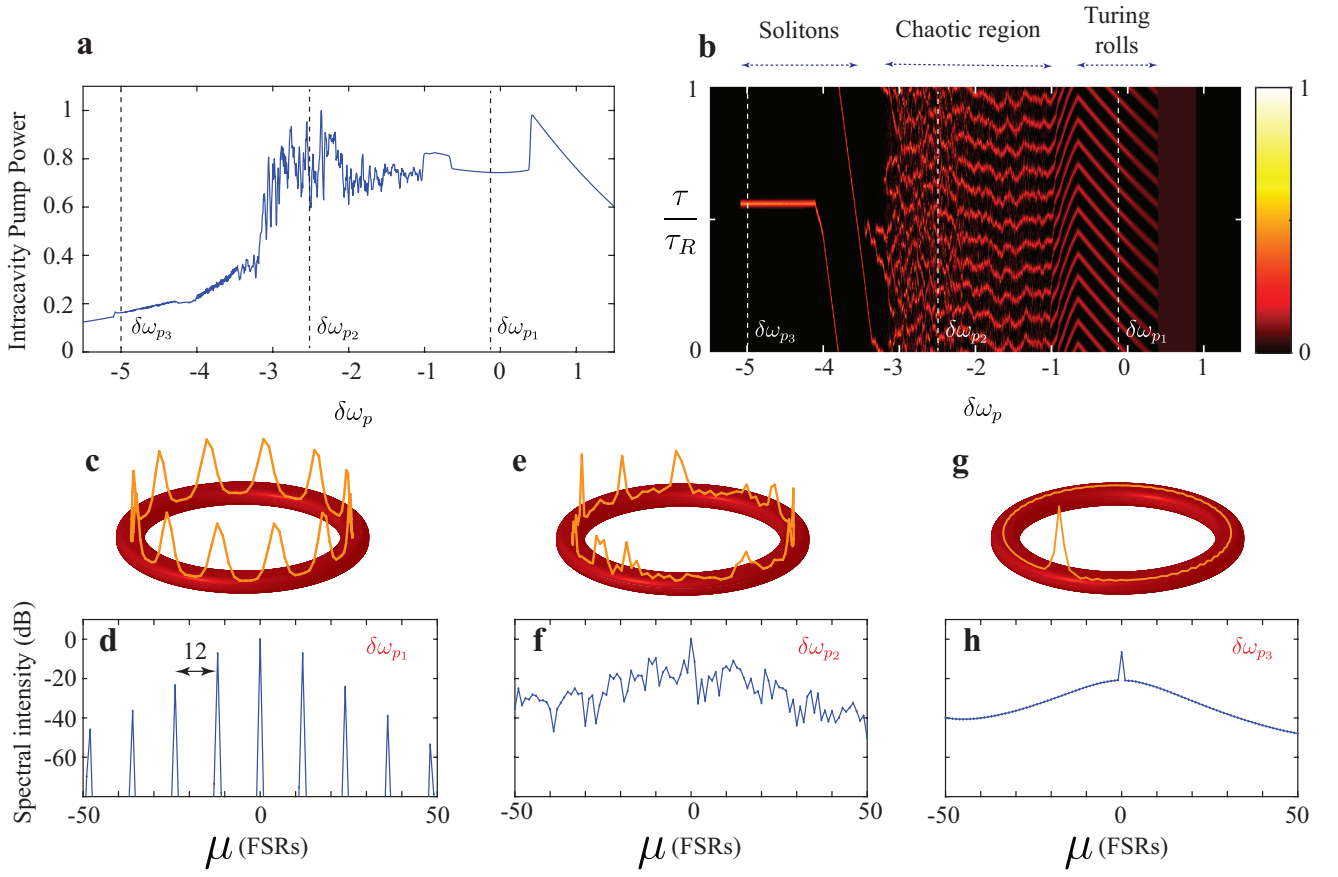


FIG. S3. **a** Pump power in the ring resonator as a function of the input pump frequency detuning  $\delta\omega_p$ , normalized by the bandwidth  $(\kappa_{ex} + \kappa_{in})$  of the all-pass filter.  $\delta\omega_p = 0$  represents the cold-cavity resonance. **b** Spatio-temporal intensity distribution in the ring as a function of the fast-time  $\tau/\tau_R$  and input pump frequency. Spatial intensity distribution and frequency comb spectrum, **c,d** in the region of Turing rolls, at  $\delta\omega_{p1}$ ; **e,f** in the chaotic region, at  $\delta\omega_{p2}$ ; and **g,h** in the region of solitons, at  $\delta\omega_{p3}$ .

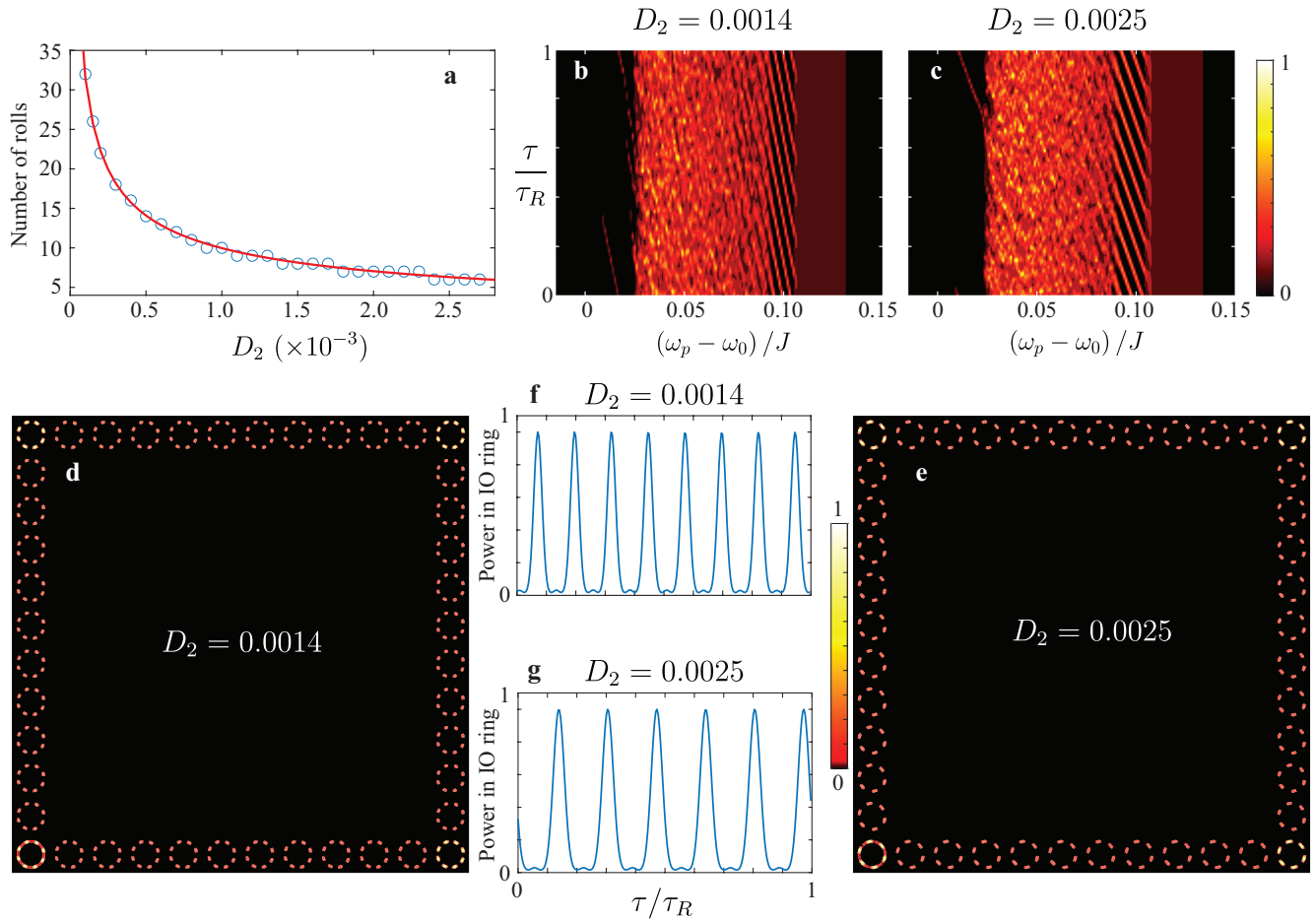


FIG. S4. **a** Number of Turing rolls in the topological frequency comb as a function of the dispersion parameter  $D_2$ . Open circles are numerically simulated values and the solid-line is a  $1/\sqrt{D_2}$  fit to the data. **b,c** Spatial intensity distributions integrated over the super-ring resonator, for  $D_2 = 0.0014$  and  $D_2 = 0.0025$ , respectively. Similar to Fig. 2d and Fig. 3a of the main text, we observe distinct regions of Turing rolls and also solitons as we tune the pump frequency. **d,e** Spatial intensity distributions in the lattice for input pump frequencies in the region of Turing rolls. The Turing rolls are phase locked throughout the edge of the lattice. **f,g** Turing rolls within a ring resonator on the edge, for the two dispersion values.

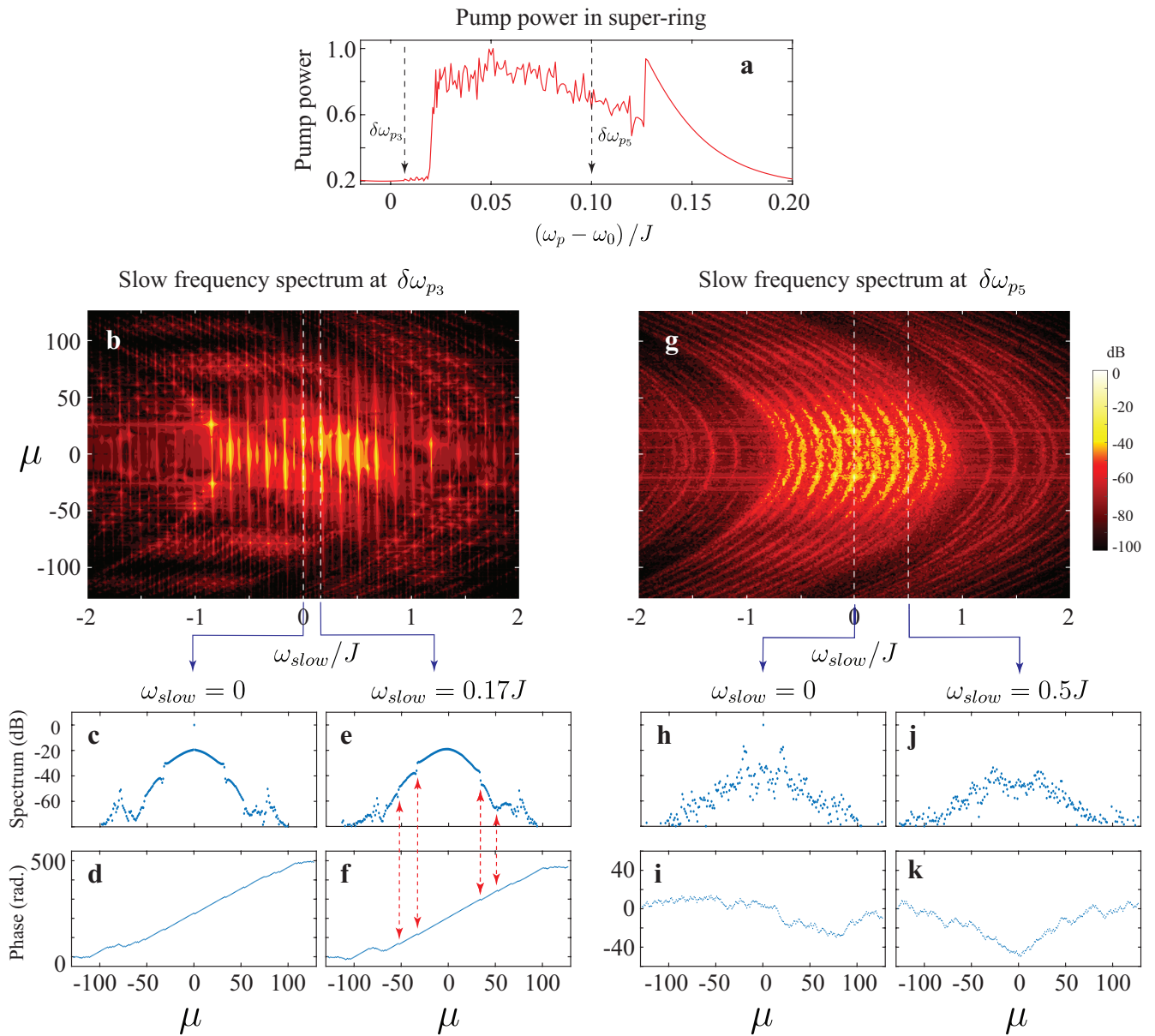


FIG. S5. **a** Total pump power in the super-ring resonator as a function of the pump frequency detuning  $\delta\omega_p$  (same as Fig. 3b of the main text, repeated here for convenience). **b** Slow-frequency spectrum in the regime of nested solitons (same as Fig. 3k of the main text). **c-f** Power spectrum and unwrapped phase of the comb along fast-frequency ( $\mu$ ), at two edge state resonances with slow-frequencies as indicated on the figure. The power spectrum is smooth, except for kinks where different edge modes interfere because of dispersion. The phase varies linearly, with phase jumps exactly at locations of kinks in the power spectrum (shown by dashed red lines). **g-k** Corresponding results for pump frequency in the chaotic regime. The comb spectrum is not smooth, and the phase varies randomly along the fast axis.

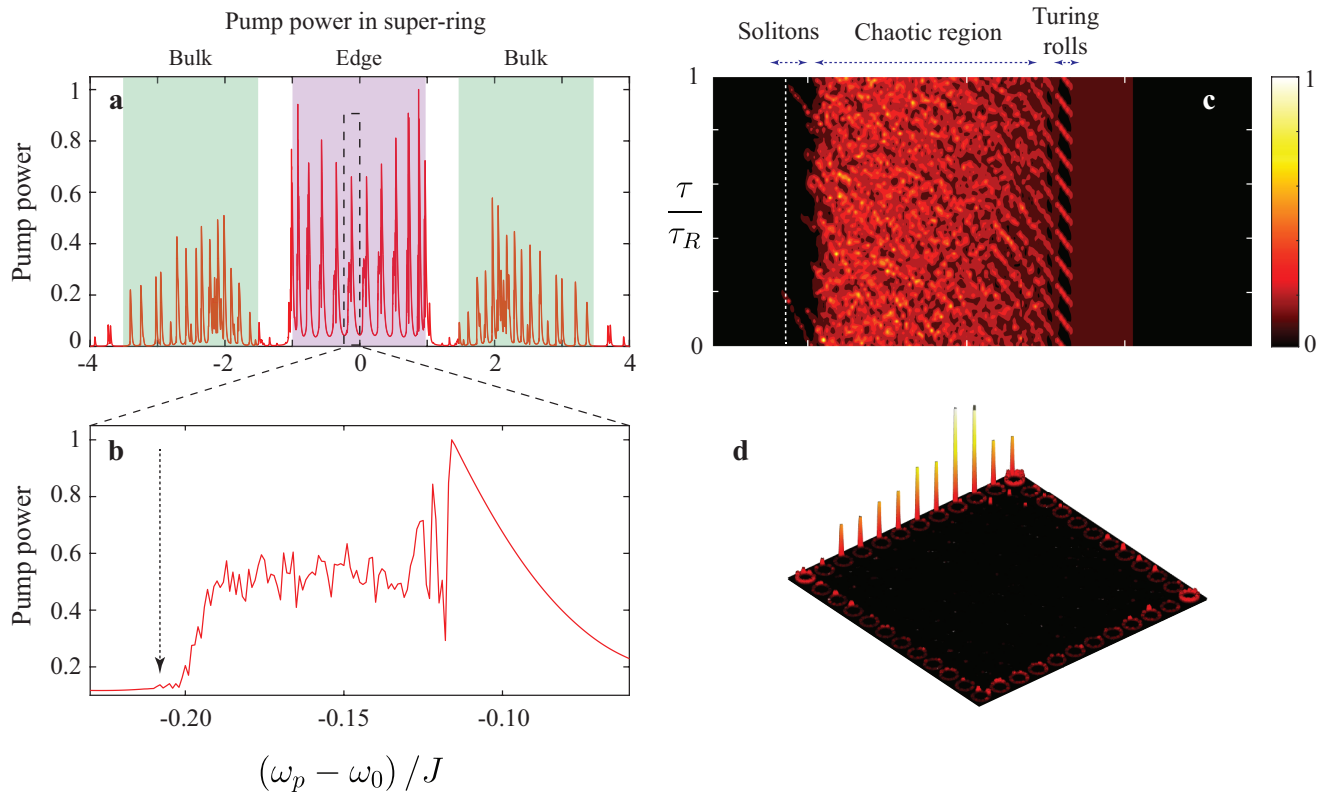


FIG. S6. **a** Total pump power in the super-ring resonator as a function of input pump frequency. **b** A zoom-in of **a** in one of the edge state resonances. **c** Spatio-temporal intensity distribution in ring resonators, integrated over all the rings in the super-ring resonator. Similar to Fig.2d and Fig.3a of the main text, the intensity distribution shows a region of phase-locked Turing rolls, a chaotic region, and a region of dissipative Kerr super-solitons. **d** Spatial intensity profile in the lattice showing a super-soliton. The input pump frequency is indicated by dashed lines in **b** and **c**.

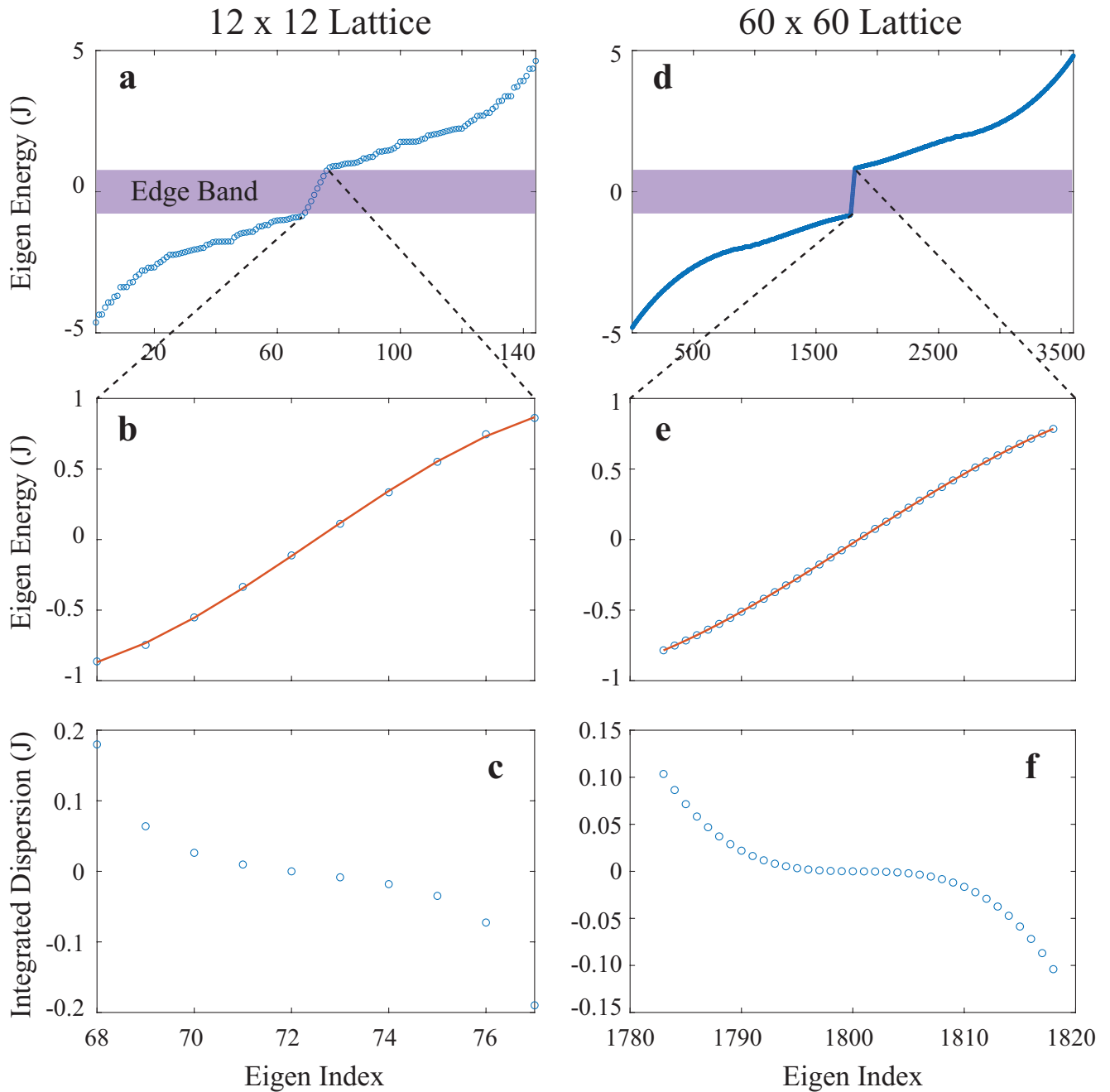


FIG. S7. **a** Energy eigenvalues for a  $12 \times 12$  lattice of (site) ring resonators in the linear regime. The edge band  $\approx (-1, 1) J$  is shaded in red. **b** A zoom-in of **a** in the edge band region. The solid-line is a third-order polynomial fit to the eigenvalues (circles). **c** Integrated dispersion of the edge state resonances, showing the predominance of third-order dispersion. **d-f** Corresponding results for a  $60 \times 60$  lattice.

**Data availability**

Source data are provided with this paper. All other data that support the plots within this paper and other findings of this study are available from the corresponding author upon reasonable request.

**Code availability**

The codes that support the findings of this study are available from the corresponding author upon reasonable request.

**Acknowledgements**

This research was supported by the Air Force Office of Scientific Research Multi-University Research Initiative (AFOSR-MURI grant no. FA9550-16-1-0323), Office of Naval Research Multi-University Research Initiative (ONR-MURI grant no. N00014-20-1-2325), United States Army Research Laboratory grant no. W911NF1920181 and NSF grant no. PHY1820938. Y.K.C. was supported by the Air Force Office of Scientific Research (AFOSR grant no. FA9550-20-1-0357).

**Author contributions**

S.M. and M.H. conceived the idea. S.M. performed the numerical simulations, analysed the data and wrote the manuscript with inputs from M.H., Y.K.C., G.M. and K.S. M.H. supervised the project.

**Competing interests**

S.M. and M.H. have filed a provisional patent based on the results reported in this manuscript.

**Additional information**

**Supplementary information** The online version contains supplementary material available at <https://doi.org/10.1038/s41567-021-01302-3>.

**Correspondence and requests for materials** should be addressed to S.M.

**Peer review information** *Nature Physics* thanks Vittorio Peano and the other, anonymous, reviewer(s) for their contribution to the peer review of this work.

**Reprints and permissions information** is available at [www.nature.com/reprints](http://www.nature.com/reprints).